

University of Tartu

Faculty of Science and Technology

Institute of Technology

Hendrik Ehrpais

# ESTCube-2 attitude and orbit control system design

Master's Thesis in Computer Engineering (30 ECTS)

Supervisor:

Andris Slavinskis, PhD

Tartu 2017

# Abstract

## **ESTCube-2 attitude and orbit control system design**

This thesis presents the design and analysis of the attitude and orbit control system for the ESTCube-2 CubeSat. The objective of the system is to spin up the satellite to high angular rates, perform accurate pointing and should also be able to operate outside of the Earth's magnetic influences, for example in a Lunar orbit.

For this thesis various requirements for the subsystem and payloads of the nanosatellite have been gathered. From these requirements the design drivers for the attitude and orbit control system are identified. Additionally the thesis analyses the ESTCube-1 nanosatellite attitude determination and control performance and presents the lessons learned, which provides input to the design of the ESTCube-2 nanosatellite.

Based on the requirements a set of actuators and sensors are presented that fulfil the various ESTCube-2 mission objectives. The thesis also covers the attitude estimation process. This is done by describing the data generation from the simulation environment and the different potential algorithms to be used for sensor fusion. A sensor fusion algorithm for nanosatellite attitude determination is proposed and the first implementation was made to work on the ESTCube-2 microcontroller. Initial results for the algorithm are described and the future improvements are identified.

**Keywords:** ESTCube-2, GNC, ADCS, AOCS, system design, sensors, actuators, algorithms, sensor fusion, UKF, UPF, Kalman filter

## **ESTCube-2 asendi- ja orbiidikontrolli süsteemi disain**

Käesolev magistritöö esitab ESTCube-2 kuupsatelliidi asendi ja orbiidi kontrolli

alamsüsteemi disaini ja analüüsi. Selle süsteemi eesmärk on panna satelliit pöörlema suurteel kiirustel, suunata satelliiti väga täpselt Maa suhtes ning võimaldada töötamist ka väljaspool Maa magnetvälja, näiteks Kuu orbiidil.

Selle töö käigus on kogutud erinevate kasulike lastide nõuded ning nende põhjal leitud asendi määramise ja kontrolli süsteemi nõuded. Nendest nõuetest on välja toodud tähtsaimad, mille põhjal süsteemi arendatakse. Lisaks analüüsitakse töös nanosatelliidi ESTCube-1 asendimääramise ja -kontrolli süsteemi tööd, kust tuuakse välja lisanõuded süsteemile.

Nende nõuete põhjal esitatakse sensorite ning aktuaatorite disain ning valik, mis täidavad ESTCube-2 nõuded. Töös on välja töödud erienvad asendi määramise algoritmid ning nendele algoritmidele testandmete genereerimise keskkond. Üks nendest algoritmidest on ise välja töötatud ning pandud tööle ESTCube-2 mikroprotsessoril. Esialgsed asendi määramise tulemused ning viisid kuidas algoritmi tööd parandada on esitatud.

**Märksõnad:** ESTCube-2, GNC, ADCS, AOCS, süsteemi disain, sensorid, aktuaatorid, algoritmid, sensor fusion, UKF, UPF, Kalman filter

**CERCS:** T320 Space Technology; P160 Statistics, operations research, programming, actuarial mathematics

# Table of Contents

|  |           |
|--|-----------|
| <b>Abstract</b>                              | <b>2</b>  |
| <b>List of Figures</b>                       | <b>6</b>  |
| <b>List of Tables</b>                        | <b>8</b>  |
| <b>Acronyms and Abbreviations</b>            | <b>9</b>  |
| <b>1 Introduction</b>                        | <b>11</b> |
| 1.1 Background . . . . .                     | 11        |
| 1.2 Thesis Objectives . . . . .              | 12        |
| <b>2 ESTCube-2 Mission and Requirements</b>  | <b>13</b> |
| 2.1 ESTCube-2 nanosatellite . . . . .        | 13        |
| 2.2 Lessons Learned from ESTCube-1 . . . . . | 16        |
| 2.2.1 Sensors . . . . .                      | 16        |
| 2.2.2 Determination . . . . .                | 17        |
| 2.2.3 Actuators and pointing . . . . .       | 19        |
| 2.2.4 Spin rate control . . . . .            | 20        |
| 2.3 Requirements . . . . .                   | 21        |
| 2.3.1 Design drivers . . . . .               | 22        |
| 2.4 Subsystem Design . . . . .               | 24        |
| <b>3 ESTCube-2 Actuators and Sensors</b>     | <b>25</b> |
| 3.1 Actuators . . . . .                      | 25        |
| 3.1.1 Reaction wheels . . . . .              | 25        |
| 3.1.2 Magnetorquers . . . . .                | 29        |

|          |  |           |
|----------|--|-----------|
| 3.1.3    | Cold gas thrusters . . . . .                                   | 30        |
| 3.2      | Sensors . . . . .  | 32        |
| 3.2.1    | Sun sensors . . . . .  | 32        |
| 3.2.2    | Other sensors . . . . .  | 34        |
| <b>4</b> | <b>Attitude Determination</b>                                  | <b>36</b> |
| 4.1      | Attitude . . . . .   | 36        |
| 4.2      | Wahba's Problem . . . . .                                      | 37        |
| 4.2.1    | Models for the satellite . . . . .                             | 38        |
| 4.3      | Sensor Modelling . . . . .                                     | 39        |
| 4.4      | Simulation Environment . . . . .                               | 41        |
| <b>5</b> | <b>Attitude Estimation Algorithms</b>                          | <b>45</b> |
| 5.1      | Kalman Filter . . . . .  | 45        |
| 5.2      | Unscented Kalman Filter . . . . .                              | 47        |
| 5.3      | Unscented Particle Filter . . . . .                            | 50        |
| 5.4      | Light Unscented Particle Filter . . . . .                      | 52        |
| 5.5      | Filter Testing . . . . .                                       | 54        |
| <b>6</b> | <b>Conclusions and future work</b>                             | <b>58</b> |
|          | <b>References</b>  | <b>59</b> |
| <b>7</b> | <b>Appendices</b>  | <b>62</b> |
| <b>A</b> | <b>Tether Deployment Calculator</b>                            | <b>63</b> |
| <b>B</b> | <b>Requirements mindmap for the AOCS subsystem</b>             | <b>64</b> |
| <b>C</b> | <b>Input for UKF vs LUPF filter tests using simulated data</b> | <b>66</b> |
| <b>D</b> | <b>Input for UKF vs LUPF filter tests with EC1 data</b>        | <b>67</b> |
|          | <b>Lihtlitsents</b>  | <b>68</b> |

# List of Figures

|     |  |    |
|-----|--|----|
| 2.1 | ESTCube-2 CAD model. From top to bottom: plasma brake and high speed communications modules; satellite bus, two Earth observation cameras, cold gas thruster module . . . . .  | 14 |
| 2.2 | ESTCube-1 following the Earth's magnetic field during the course of two orbits. [1] . . . . .  | 20 |
| 2.3 | Limited pointing capabilities achieved with ESTCube-1. The noise is mostly caused by spikes in the attitude determination output not by attitude control. [1] . . . . .  | 20 |
| 2.4 | Spin-up of the satellite to 841 deg/s. The spin-up is performed in many steps over one month with gaps in between for charging the batteries [1].  | 22 |
| 2.5 | The figure describes the AOCS subsystem and the various modules that it involves. . . . .  | 24 |
| 3.1 | ESTCube-2 subsystem compartment, where it is possible to see the reaction wheels close to the cutouts from the PCBs. . . . .   | 27 |
| 3.2 | Thruster module for ESTCube-2. The thrusters used for spinning up the satellite around x-axis are designated with red arrows. The tank is the large circular structure that holds fuel. . . . .  | 32 |
| 3.3 | Diffraction calculation for Sun sensors. Top plot shows when light illuminates the end of the sensor and the bottom plot when the light illuminates the middle of the sensor. All of the wavelengths from 300 to 1000 nm are integrated together. Currently the sensor optical response is not taken into account. The x-axis represents the sensor length from -1 to 1 with each cross on the image representing one pixel on the sensor and the y-axis represents the intensity for each pixel from 0 to 1 . . . . . | 34 |

|     |  |    |
|-----|--|----|
| 4.1 | The simulation environment collapsed view with various models. The simulation environment given in this Figure is still under development . . .  | 42 |
| 5.1 | The Kalman filter workflow. . . . .  | 46 |
| 5.2 | The Unscented Kalman filter workflow. . . . .  | 48 |
| 5.3 | The Unscented Particle filter workflow. . . . .  | 51 |
| 5.4 | The Light Unscented Particle filter workflow. . . . .  | 53 |
| 5.5 | The Light Unscented Particle filter results. Each state vector component and the difference with the actual value. The final graph shows the RMS error for all the state vector variables. . . . . | 55 |
| 5.6 | The quaternion elements estimated from the ESTCube-1 sensor data by the LUPF algorithm. . . . .  | 56 |
| 5.7 | The difference between the quaternions from the LUPF and UKF algorithms based on ESTCube-1 sensor data. . . . .  | 57 |

# List of Tables

|     |   |    |
|-----|---|----|
| 3.1 | Reaction wheel properties from different providers . . . . .        | 28 |
| 3.2 | Magnetorquer parameters for short side and long side coils. . . . . | 30 |

# Acronyms and Abbreviations

**ADCS** attitude determination and control subsystem

**AOCS** attitude and orbit control subsystem

**IMU** inertial measurement unit

**LEO** low Earth orbit

**PCB** printed circuit board

**E-sail** electric solar wind sail

**OBCS** on-board computer system

**MCU** microcontroller

**NDVI** normalised difference vegetation index

**MEMS** microelectromechanical systems

**I2C** inter-integrated circuit

**UKF** Unscented Kalman filter

**RPM** revolutions per minute

**FOV** field of view

**ECI** Earth-centered inertial

**SGP4** Simplified Perturbations model 4

**NIR** near-infrared

**SPI** serial peripheral interface

**FPU** floating-point unit

**COTS** commercial off-the-shelf

**PSD** position sensitive device

**RMS** root mean square

# 1 Introduction

This thesis describes the analysis and design and analysis of the attitude and orbit control subsystem (AOCS) for the ESTCube-2 nanosatellite. The thesis builds on the experience gained from the ESTCube-1 project in order to design an AOCS for the ESTCube-2 CubeSat. The design is motivated by the need to have high performance pointing, high spin rate control and the ability for the satellite to perform these operations outside of the Earth's magnetic field influence [2, 3]. The thesis gathers and explains the requirements needed to fulfil various mission objectives, presents the design and selection of sensors and actuators and describes the attitude determination algorithms. The engineering model of the satellite will be integrated in late summer 2017 and by that time all of the components described in this thesis are expected to have fully functional prototypes.

The results of the thesis will be presented in an upcoming conference Recent Advances In Space Technology and after finishing the satellite the full system design is planned to be published by the author in a scientific journal. The thesis does not cover attitude control algorithms, the inertial measurement unit (IMU) selection or the electronics design of the subsystem which will be covered by other theses. The author is also the team lead for the ESTCube-2 AOCS.

## 1.1 Background

As CubeSats are becoming more used in commercial and scientific missions the requirements for the satellite platform are becoming more strict. The main limiting factor for many nanosatellite missions is usually the AOCS. Missions that have high requirements on the AOCS include Earth observation or other camera payloads [4],

laser communications [5], tether deployment [6], proximity operations [7] and others [8]. The biggest obstacle has been attitude determination and therefore pointing accuracy, which often requires larger systems than fit in a CubeSat. Recent developments in both actuators and sensors are enabling better pointing capabilities for example in the BRITE constellation [9].

However further miniaturisation and showing similar pointing performance to the BRITE constellation with a CubeSat is still necessary. In addition the high spin rate control of nanosatellites for tether deployment is shown only with limited capabilities and needs a different approach for satellites outside low Earth orbit (LEO) [1]. The AOCS design for ESTCube-2 aims to achieve high pointing accuracies and demonstrate capabilities for centrifugal tether deployment in a future Lunar mission.

## 1.2 Thesis Objectives

There are two main outcomes of the thesis: an AOCS design for the ESTCube-2 nanosatellite and a novel sensor fusion algorithm running on an embedded system that calculates the attitude of the satellite. The more detailed list of objectives is given below:

- Gather mission and payload requirements for ESTCube-2,
- Analyse the ESTCube-1 ADCS performance and gather the lessons learned,
- Define the requirements for the AOCS that fulfil the mission requirements set by the payloads,
- Describe the attitude determination process. Present algorithms to be used for nanosatellite attitude determination and their performance. Present a novel algorithm for nanosatellite attitude determination.

## 2 ESTCube-2 Mission and Requirements

This chapter describes the ESTCube-2 nanosatellite, the lessons learned from ESTCube-1 mission, the various payloads on board and the requirements and design drivers of the AOCS.

### 2.1 ESTCube-2 nanosatellite

ESTCube-2 is a 3U CubeSat built by the Estonian Student Satellite Foundation that brings together students from Estonian universities and around the world. The main aim of the CubeSat is to test technologies, such as the plasma brake, Earth observation imagers, high speed communication, cold gas propulsion, corrosion resistant coatings and the whole newly designed satellite platform [2] itself. The satellite is built with the goal to use the satellite platform outside the Earth's magnetic field for example in lunar orbit. The satellite is shown in Figure 2.1.

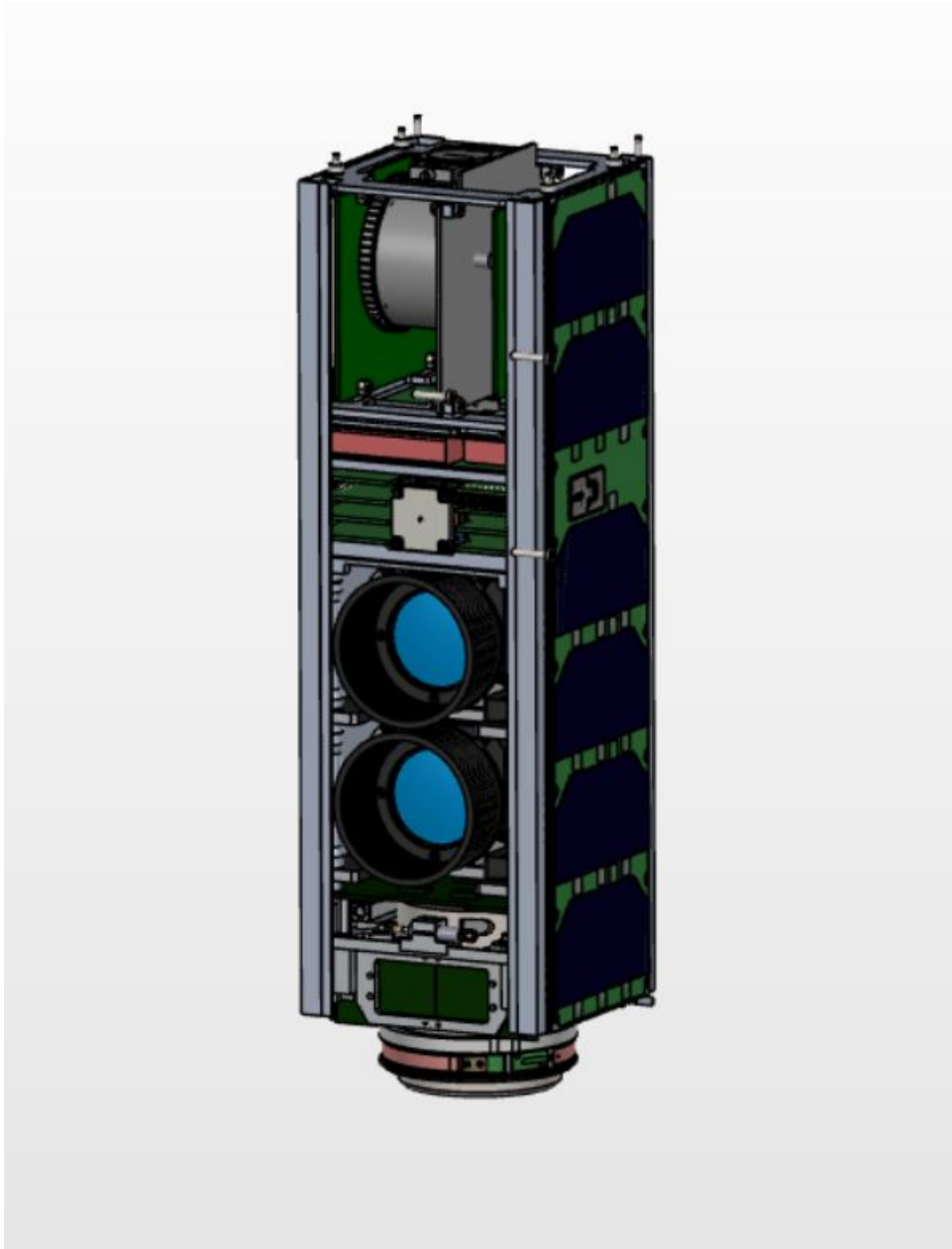


Figure 2.1: ESTCube-2 CAD model. From top to bottom: plasma brake and high speed communications modules; satellite bus, two Earth observation cameras, cold gas thruster module

Plasma brake is a technology which is based on Coulomb drag propulsion. Coulomb drag propulsion also includes electric solar wind sail (E-sail). Plasma brake can be used to de-orbit satellites under 1000 kg from LEO [10]. The same technology with minor differences can also be used as propulsion for interplanetary travel of smaller spacecraft

when taken outside of the Earth's magnetic field influence which is around a half of the Moon's distance from the Earth [11, 12, 13, 14].

The satellite carries two earth observation cameras, which aim to take measurements similar to Sentinel-2 data. If the camera performance is sufficient then they can be used to increase the Earth observation measurement frequency. The cameras will take measurements in at least two wavelength bands — visible (650-680 nm) and near-infrared (NIR) (855-875 nm) — which roughly match the two Sentinel-2 bands (4 and 8b) that can be used for validating the cameras [15]. These measurements can be used to calculate the normalised difference vegetation index (NDVI) that can be used to estimate the amount of green vegetation for agriculture. [16].

High speed communications is a C-band based module developed by Ventspils University College. Its main application is to transmit payload data from the satellite to the ground. The C-band antenna is directional and only works when it is directed towards a ground station. Because of this the satellite platform also has a more versatile communication system that has a wider radiation pattern, but lower speeds.

The corrosion resistant coating experiment will test the degradation of two wires in the space environment mostly caused by atomic oxygen. One of the wires will be coated using atomic deposition methods developed in University of Tartu in cooperation with Captain Corrosion OÜ. The change of resistance of the wires will be measured and compared to each other during the satellite's lifetime.

A Swedish company Nanospace AB provides ESTCube-2 with a cold gas propulsion module. The module will be described together with other actuators in Section 3.1. The main goal of the system is to enable attitude control and tether deployment outside of the Earth's magnetic influence.

The ESTCube-2 mission and satellite design was presented at Small Satellites Systems and Services Symposium by the author. Additional details on the mission can be found in a conference paper [3]. The major difference is that the laser communication was dropped from ESTCube-2.

## 2.2 Lessons Learned from ESTCube-1

In order to design the AOCS for the ESTCube-2 satellite it is necessary to describe what we learned from the previous mission, ESTCube-1. ESTCube-1 was a nanosatellite developed by students from different Estonian universities including University of Tartu, Tallinn University of Technology, Estonian University of Life Sciences, Estonian Aviation Academy. ESTCube-1 was a 1-U CubeSat with the main scientific mission to use centrifugal force to deploy an E-sail tether that is then charged [6]. The electrostatic tether interacts with the Earth's plasma and the effect on the satellite is measured [17].

The satellite platform was tested in space, however the tether deployment was unsuccessful because the motor that releases the tether did not work in orbit, most likely due to launch vibrations [18]. The results of ESTCube-1 and its attitude determination and control subsystem (ADCS) have been presented in various articles and the ADCS results and insights for the next satellite design are described in sections below [19, 20, 21, 1, 22].

### 2.2.1 Sensors

The ESTCube-1 attitude determination was done by three different types of sensors, magnetometers, Sun sensors and gyroscopes. The sensors performed well enough to fulfil most of the mission requirements, however significant accuracy improvements could be made by implementing various fixes, some of which were performed using in-orbit updates to the software handling sensor measurements.

One of the main results was to perform temperature and offset calibration for magnetometers and gyroscopes during the mission [22]. This is required because there can be changes to the residual magnetic moment of the satellite and microelectromechanical systems (MEMS) based gyroscopes are affected by a drift in output over time [23]. In addition to offset calibration we performed a temperature calibration of the sensors – the main outcome was that for temperature calibration both the offset and sensor gain calibrations are required and the calibration can be non-linear.

**Additional temperature calibration should be made and in addition an in-orbit calibration method should be developed pre-launch.**

Our calibration functions developed for the Sun sensors did not work as expected because of two reasons: a drift in the reference voltage of the sensors and the fact that the sensors were calibrated by scanning the sensors in one dimension. The sensor response linearity is dependent on the intensity of the light reaching the sensor and this non-linearity was the main thing to compensate for in the calibration. However, by changing the angle of the incident light in two dimensions, less light reaches the sensor which reduces the non-linearity. Because this was not taken into account, the calibration functions made could not be used.

**Calibrations for ESTCube-2 will use a different style of test benches and a different approach to Sun sensors, which helps reduce the issue of non-linearity on the sensor.**

Another important factor was that inter-integrated circuit (I2C) based sensors created difficulties for sensor data processing. Sensors started outputting measurements with spikes to random values and in addition to ruining the data for those sensors, it also influenced other sensors on the same I2C bus. Over time this problem became worse, most likely because of the degradation of sensors in orbit.

**This issue led us to use serial peripheral interface (SPI) sensors for next missions, as they are easier to configure and debug.**

## **2.2.2 Determination**

The attitude determination part of the system is done using sensor fusion. The results from the sensors are taken and the orientation of the satellite in the form of a quaternion is found for every time step. On ESTCube-1 this was handled using an Unscented Kalman filter (UKF), which is further explained under Section 5.2. The satellite encountered various problems with attitude estimation.

During in-orbit validation of the attitude determination process we encountered the issue that we had two different versions of the attitude determination software. One of

the versions was written in MATLAB and the other version was the on-board software in C language. The main problem was that syncing up the changes between the two environments became increasingly difficult and at one point there was no advantage to testing with the simulation environment any more, because it had inferior performance to the on-board software. This created issues when simulation of different conditions was required and we were not able to simulate it properly. In addition, before launch the code was written in MATLAB and porting it to an embedded system was time-consuming and introduced some bugs that needed additional troubleshooting.

**To fix this issue in future missions we are planning to use C code wrappers in our MATLAB/Simulink simulation environment that would use the on-board software to run inside the simulation environment. This will prevent two different versions of the software and make porting the code easier.**

The covariance matrices used by the UKF are hard to optimise, because the conditions in space differ from operations on the ground. If you try to optimise the matrices based on laboratory measurements, then it is possible that because the sensor results are either more or less accurate than initially tested, the covariance matrices are not optimal and the attitude determination will perform worse than expected.

At the same time we do not have a good reference for attitude when the satellite is in orbit. On ESTCube-1, we used images taken by the satellite as references by analysing the images for landmarks [22]. In ESTCube-2 we can use the star tracker for attitude verification, however both of these approaches do not work at higher spin rates and with high frequency.

**We aim to optimise the covariance matrices in-orbit constantly using a different method, for example a genetic algorithm [24].**

There are many types of sensors used and there are 3 to 4 sensors from each type. As we are rotating very fast any difference in the exact timing of the sensor can produce a phase shift. For example, if we are rotating at 500 deg/s, a 2 ms difference in sensor measurements results in a 1 degree phase shift between the sensors.

**It is important to both know the exact timing when the sensor measurements are taken and all of the sensor measurements should be interpolated to the**

**exact same time.**

It was possible to run the UKF 10 times per second using the STM32F1 MCU at 32 Mhz. The frequency of updating the attitude and the control signal of the satellite was good enough for high spin rate control.

**As we are planning to use a STM32F7 which is able to provide up to 216 Mhz and has a floating-point unit (FPU), then it is possible to try to include more computations into the filter, which means it is possible to use more complex filters.**

### **2.2.3 Actuators and pointing**

The ADCS was most affected by the residual magnetic moment affecting the satellite. The magnetic moment was around  $0.1 \text{ Am}^2$  [1]. This magnetic moment generates torque if not aligned with the Earth's magnetic field which means that during an orbit when the magnetic field changes there are almost always torques affecting the satellite. If it is not possible to compensate the magnetic field, then stable pointing becomes impossible. The effect of the ESTCube-1 satellite following the magnetic field during two orbits is described in Figure 2.2. **No ferromagnetic materials shall be used on the satellite.**

As the strength of the magnetic coils was also close to  $0.1 \text{ Am}^2$  [20] then it was not possible to fully compensate for the magnetic field and control the satellite at the same time. In addition, the power generation was not high enough to compensate for the magnetic field all the time because of the degrading solar panels [18]. This resulted in the satellite not achieving stable pointing continuously. The pointing result achieved is shown on Figure 2.3.

**The maximum magnetic moment from the magnetic coils should be larger in case there are any issues on ESTCube-2 with magnetic materials.**

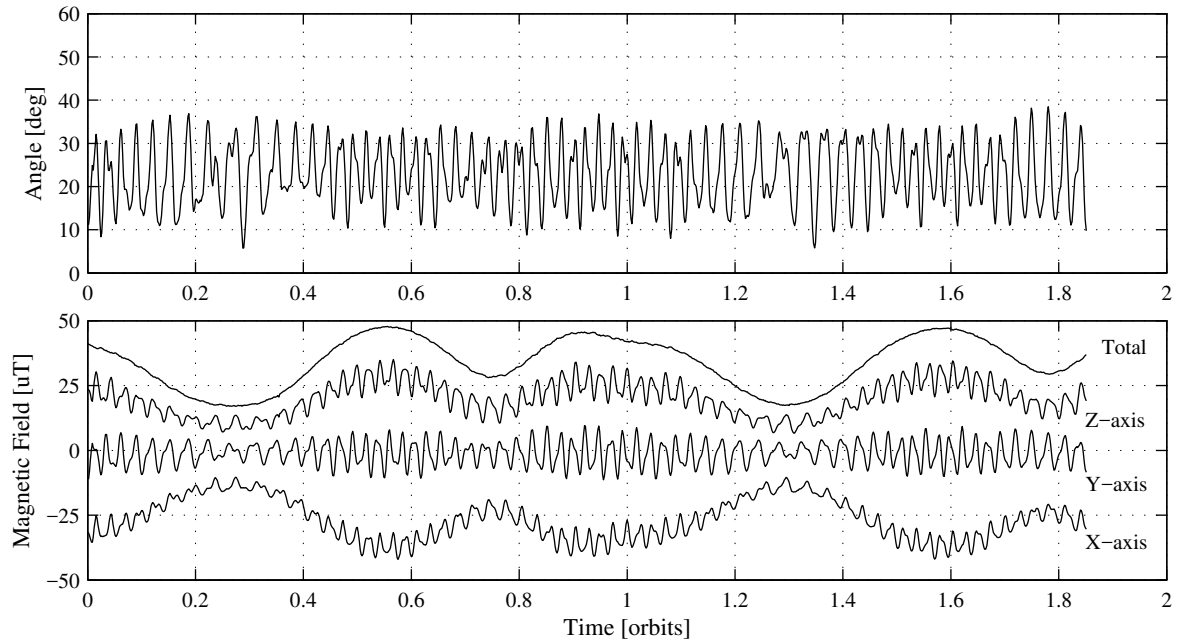


Figure 2.2: ESTCube-1 following the Earth’s magnetic field during the course of two orbits. [1]

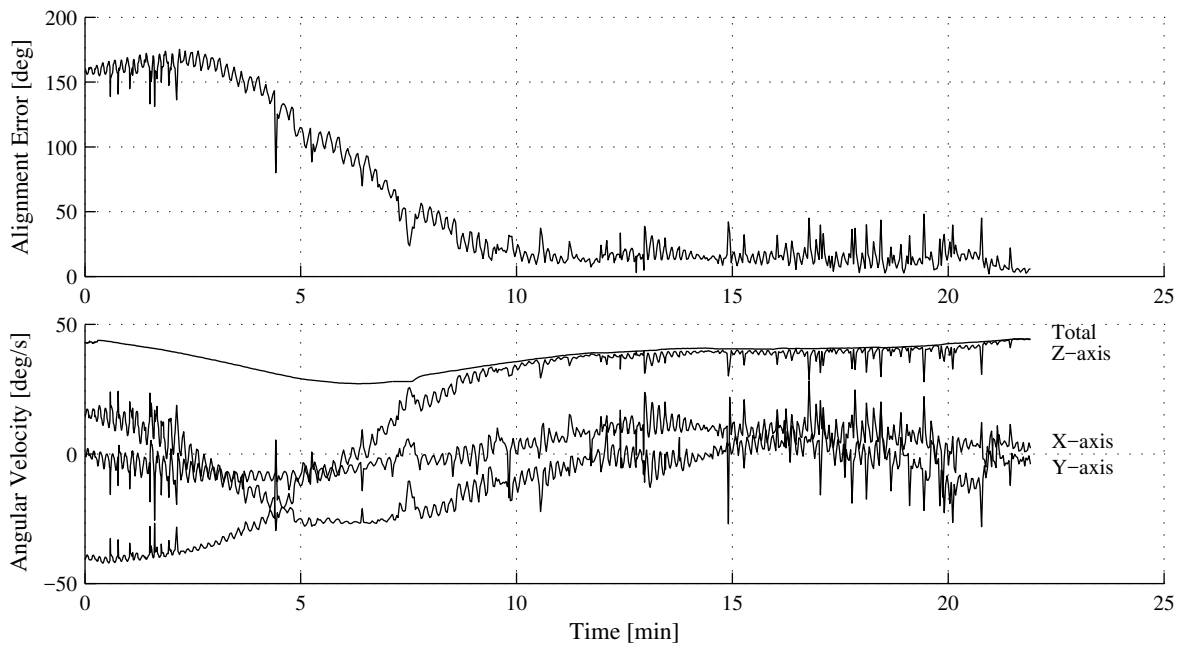


Figure 2.3: Limited pointing capabilities achieved with ESTCube-1. The noise is mostly caused by spikes in the attitude determination output not by attitude control. [1]

## 2.2.4 Spin rate control

With ESTCube-1 we were aiming to achieve high spin rates of up to  $360 \text{ deg/s}$  using magnetic control [19]. To achieve those spin rates, the control loop has to run in a

small amount of time because while rotating, the Earth’s magnetic field in the satellite inertial reference frame changes that causes the control signal not to be correct. The same problem occurs if we are trying to align the tether deployment axis with the Earth’s polar axis.

**Because of this the determination and control loop has to work at least at 10 hz.**

There are some countermeasures one can take to optimise the control signal. The aim is to run the coils almost all the time so the control signal would be around 90 ms long at 10 hz. However, during that time there will be a considerable phase shift at higher angular velocities and to compensate for that the control signal needs to be altered. Although the ideal case would be a more accurate function, in ESTCube-1 we extrapolated the control signal to the middle of the control period so 45 ms into the future, which would mostly eliminate the problem of accumulating errors from phase shift, but still make the control less efficient.

**The phase shift problems for controlling the satellite at high spin rates need to be considered and compensated for by changing the control signal.**

Using the optimisations for the control algorithms, compensation for magnetic influences and improvements to the attitude determination process ESTCube-1 achieved the highest controlled spin rate of a satellite known to the author of 841 deg/s [1]. The spin-up process is shown on Figure 2.4. The results of the attitude control on ESTCube-1 has been published by the thesis author in Acta Astronautica titled “Nanosatellite spin-up using magnetic actuators: ESTCube-1 flight results.”

## 2.3 Requirements

A set of mission and payload requirements were gathered in order to describe the system and subsystem requirements. The requirements will be presented from the AOCS design point of view and only the design drivers for the system will be explained in detail. A more comprehensive set of requirements can be found in a mind map shown in Appendix B.

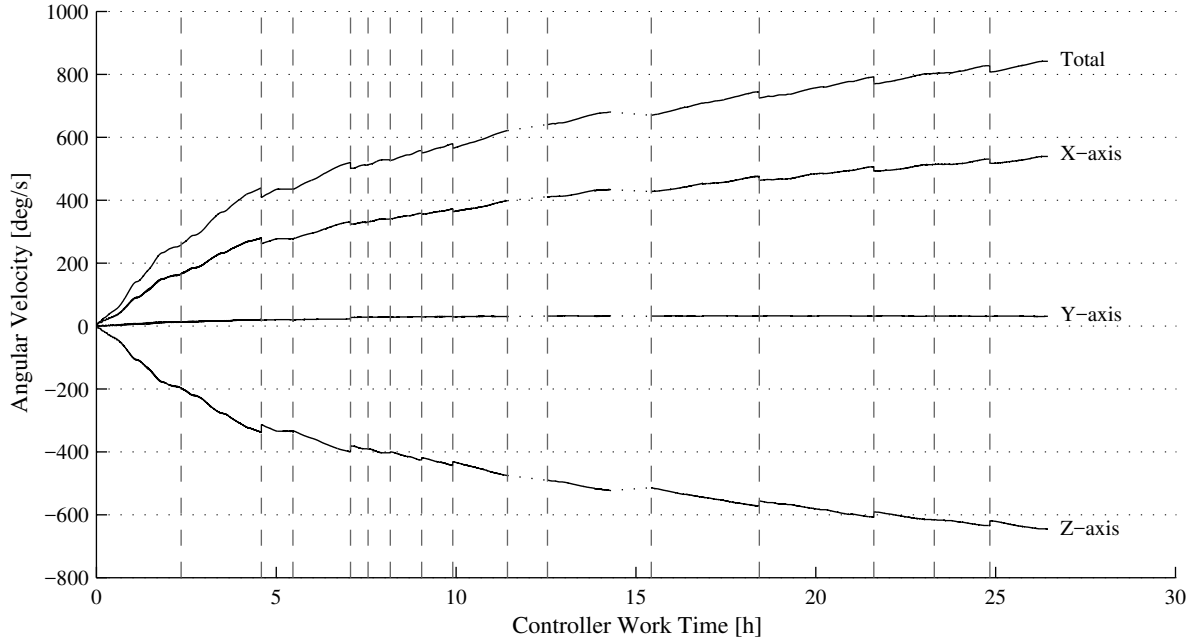


Figure 2.4: Spin-up of the satellite to 841 deg/s. The spin-up is performed in many steps over one month with gaps in between for charging the batteries [1].

### 2.3.1 Design drivers

To test the electric solar wind sail in LEO, the satellite needs to spin itself up in order to generate centrifugal force on the endmass of the tether to keep the tether under tension, which prevents the tether from getting tangled [17]. To deploy 100 *m* of tether which is the minimum requirement it is required to generate 6.29 *Nms* of angular momentum with the satellite. The tether angular momentum calculations are shown in Appendix A. Because of the high angular momentum requirements, the tether deployment has to occur in steps, this means that the system has to be able to spin itself up while the tether is already deployed, which puts a limit on the angular acceleration allowed after the tether deployment. The first deployment will deploy 10 metres of tether in order to test the electron emitters for the Lunar orbit mission.

It is necessary to keep the spin axis and Earth's polar axis aligned to measure the plasma brake effect on the satellite. The maximum allowed alignment error between the Earth's polar axis and the satellite's rotation axis is 3 degrees.

The Earth Observation camera requires very high pointing ability and ground tracking.

The aim of the ground tracking is to combine the different wavelength informations from the camera and merge them into one image. The pointing stability shall be under 0.125 deg/s and should be under 0.025 deg/s so that the pixels would not become blurry during the exposure time of the camera. The required absolute pointing error accuracy is up to 0.25 deg, which would be sufficient to do ground tracking with the current camera design.

To be able to operate in a Moon orbit, the satellite has to determine the attitude without magnetometers, control the attitude without electromagnetic coils and the bandwidth for software updates is limited and has a delay. The Moon mission requires cold gas propulsion and star trackers in order for the satellite to be able to perform AOCS. For the Moon mission the algorithms have to work on their own and the calibration of sensors and the calibration of the sensor fusion should be done automatically when possible.

The AOCS will use the microcontroller (MCU) of the on-board computer system (OBCS), which means that the interfaces for the sensors and actuators are defined and that the sensor and actuator electronics needs to be compatible.

## 2.4 Subsystem Design

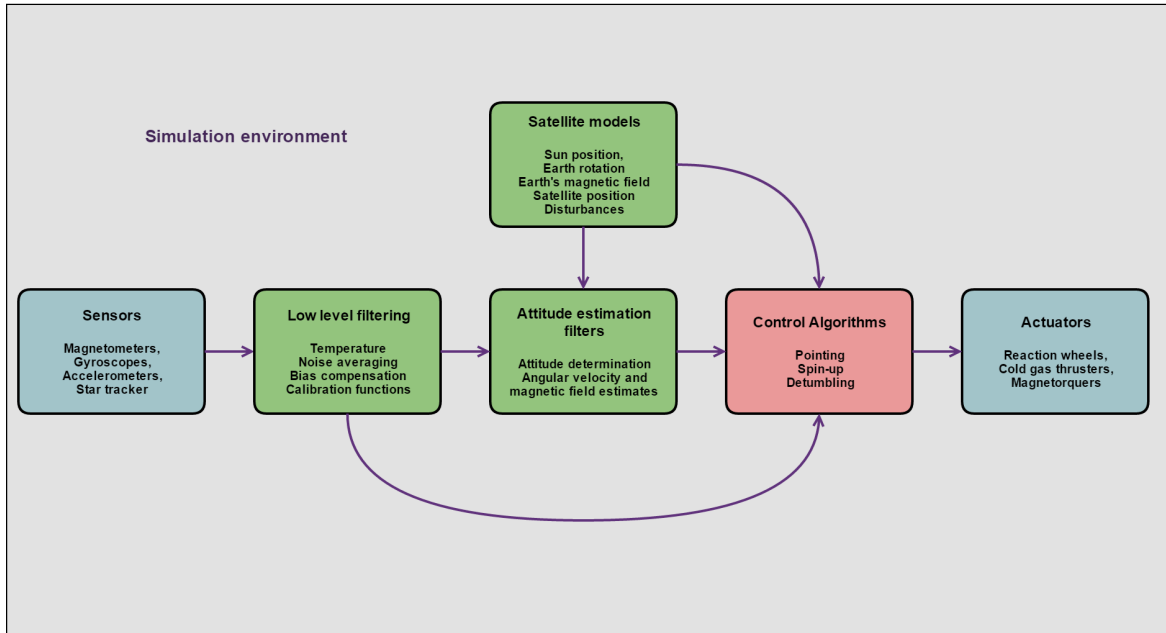


Figure 2.5: The figure describes the AOCS subsystem and the various modules that it involves.

The attitude determination and control is composed of various different modules that are described in Figure 2.5. From the modules described on the figure, this thesis describes Sun sensors and actuators for ESTCube-2, the simulation environment with the corresponding satellite models and sensor noises that are necessary for testing attitude estimation and the attitude estimation filters. The details of the various blocks are explained in the further chapters.

## 3 ESTCube-2 Actuators and Sensors

This chapter describes the sensors and actuators chosen and designed for ESTCube-2 and why they were chosen. There are three actuators: reaction wheels, magnetorquers and cold gas thrusters. There are various sensors such as star trackers, IMUs and Sun sensors, but only Sun sensor design is covered in detail in this thesis.

### 3.1 Actuators

#### 3.1.1 Reaction wheels

Reaction wheels are actuators that can be used to change the angular velocity of the satellite. An electric motor spins up a flywheel to a specified revolutions per minute (RPM), which causes the satellite to rotate in the opposite direction due to the conservation of angular momentum. By increasing the angular velocity and the mass of the flywheel compared to the rest of the satellite's mass, angular velocity of the satellite changes. This relationship is described in Equation 3.1, where  $\mathbf{I}_s$  is the satellite's inertia,  $\mathbf{I}_w$  is the reaction wheel's inertia,  $\omega_s$  is the satellite's angular velocity and  $\omega_w$  is the wheel's angular velocity.

$$\mathbf{I}_s\omega_s = -\mathbf{I}_w\omega_w \quad (3.1)$$

Reaction wheels are typically used on CubeSats to achieve high pointing accuracies compared to other actuators. The RPM of the reaction wheels can be adjusted at

very high resolution and therefore the reaction wheels are ideal for keeping the satellite pointed at one specific target. Reaction wheels are also optimal for slew manoeuvres, because after the manoeuvre it is possible to remove the change in reaction wheel speed that was generated, which will stop the rotation of the satellite.

However, reaction wheels are limited by their total amount of angular momentum storage and the maximum torque generated. As the volume in a CubeSat is very limited, then the wheels used in nanosatellites are very small and the total angular momentum generated is also small. This means that for high spin rate control we require other means of angular momentum generation.

Three reaction wheels are placed on each satellite axis that enables the control of the satellite's spin rate in those three axes. The reaction wheels are placed in the cutouts made in the printed circuit board (PCB) of the satellite bus as shown on Figure 3.1.

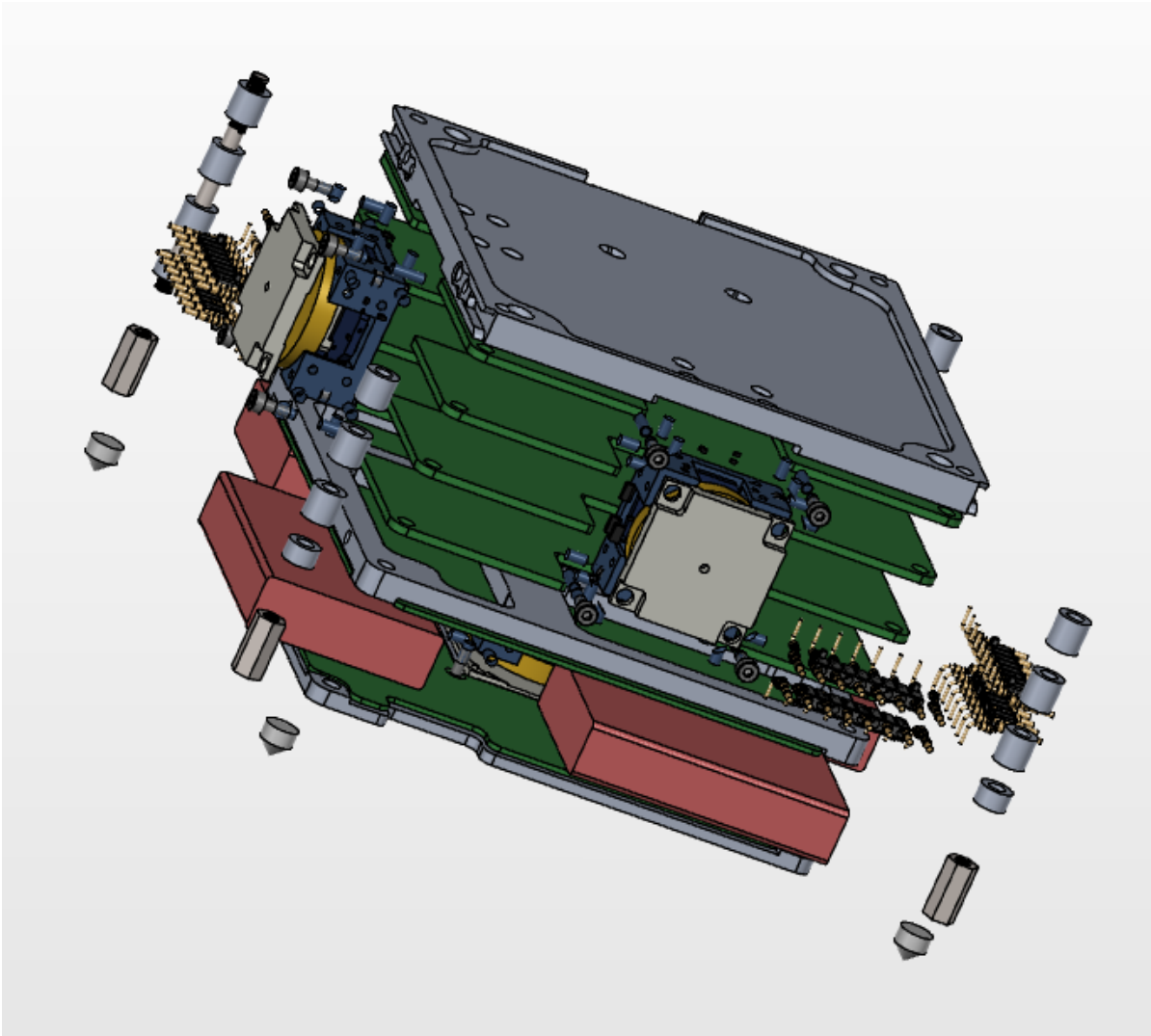


Figure 3.1: ESTCube-2 subsystem compartment, where it is possible to see the reaction wheels close to the cutouts from the PCBs.

Because of the high RPM of the flywheels, any small manufacturing errors cause jitter in the reaction wheel. The jitter results in perturbations of the attitude and extra angular velocity in unwanted directions. This combined with misplacement of the reaction wheels needs to be compensated when operating the wheels. However, compensating for this causes the wheels to get saturated over time. When the wheels are saturated they can not be used to increase/decrease the angular velocity of the satellite in a certain direction any more. Because of this, reaction wheels are usually used in combination with a different actuation method that can be used to unload the wheels. The wheels stored momentum is released while the torque generated by this operation is compensated with a different

actuator.

As gyroscopic sensors based on MEMS technology are highly influenced by various jitters, then using reaction wheels with considerable jitter limits the performance of the attitude determination of the satellite.

As the reaction wheels need precise manufacturing in order to be usable and because mechanical engineering is not the main expertise of the ESTCube team, we decided to order the reaction wheels from a commercial provider. Three different providers were chosen for further analysis: Sinclair interplanetary, Astrofein and Hyperion Technologies.

Different options were considered and the Hyperion Technologies reaction wheels were chosen to be used on the ESTCube-2 nanosatellite. The decision was made by comparing different parameters of the wheels presented in Table 3.1, where the main considerations were the torque, momentum storage and size. By choosing the RW210.15 we are able to integrate the reaction wheels into the same compartment as the rest of the satellite subsystems and free up space for payloads.

| Provider/model                       | Total momentum storage           | Torque                         | Dimensions per wheel                | Price per wheel | notes  |
|--------------------------------------|----------------------------------|--------------------------------|-------------------------------------|-----------------|--|
| Astrofein RW1 [25]                   | $5.8 \cdot 10^{-4} \text{ Nm s}$ | $23 \cdot 10^{-6} \text{ Nm}$  | $21 \times 21 \times 21 \text{ mm}$ | 6000 <i>e</i>   | Separate electronics to drive the wheel motor is required            |
| Hyperion technologies RW210.15 [26]  | $1.5 \cdot 10^{-3} \text{ Nm s}$ | $0.1 \cdot 10^{-3} \text{ Nm}$ | $25 \times 25 \times 15 \text{ mm}$ | 9000 <i>e</i>   | Possibility to get an additional wheel for testing. Our final choice |
| Sinclair Interplanetary RW-0.01 [27] | $1 \cdot 10^{-2} \text{ Nm s}$   | $1 \cdot 10^{-3} \text{ Nm}$   | $50 \times 50 \times 30 \text{ mm}$ | 2000 <i>e</i>   | Most reliable and proven   |

Table 3.1: Reaction wheel properties from different providers

Each of the three chosen reaction wheels can generate  $0.1 \text{ mNm}$  of torque and store  $1.5 \text{ mNm s}$  of angular momentum. Maximum power consumption of each wheel is up to  $850 \text{ mW}$  and the average power consumption at the maximum RPM of 10000 is  $230 \text{ mW}$ . The dimensions of each wheel are  $25 \times 25 \times 15 \text{ mm}$  and they weigh up to  $21 \text{ g}$ . [26]

### 3.1.2 Magnetorquers

Magnetorquers are electromagnets that can be used to orientate the satellite and are one of the three actuators used on-board ESTCube-2. By generating a magnetic field on-board a satellite it interacts with the Earth's magnetic field and generates torque that aims to align both magnetic field vectors. This relationship is described in Equation 3.2, where  $\boldsymbol{\tau}$  is the generated torque,  $\boldsymbol{\mu}$  the generated magnetic field by the satellite and  $\boldsymbol{B}$  the external magnetic field vector. Because of this equation it is not possible to generate torque around the magnetic field vector if it is constant, which means that in some situations one of the axis of the satellites can become uncontrollable. This can become a problem if there is a strong magnetic field present on the satellite that follows the Earth's magnetic field.

$$\boldsymbol{\tau} = \boldsymbol{\mu} \times \boldsymbol{B} \quad (3.2)$$

The two main categories of magnetorquers are air coils and torque rods. The main advantage of the rods is that due to the ferromagnetic cores for magnetic rods, there is a stronger magnetic field generated with the same amount of current consumed compared to an air coils. However, the ferromagnetic cores can become permanently magnetised, which results in a residual magnetic moment inside the satellite. The effects of that are described under Subsection 2.2.3 and based on that experience we want to avoid it if possible.

The main advantage of the air coils is that they don't have ferromagnetic cores and that they are usually planar. Depending on the design of the nanosatellite the planar shape of the coils can be a disadvantage, but because we have full control of structure of the satellite, then the coils can be placed in a way that saves space on the satellite. In the CubeSat standard [28], there is an option to extend the side panels of the satellite from the standard PCB size. In our design we can fit the air coils inside this additional space, therefore we are able to save space inside the rest of the satellite by using air coils.

The main parameter to optimise for is the maximum magnetic dipole moment generated by the coils. We need around  $0.4 \text{ Am}^2$  of magnetic moment based on each axis. This is

based on two main factors. One is the compensation of the residual magnetic moment of the satellite, which in the ESTCube-1 case was around  $0.1 \text{ Am}^2$ . This would leave  $0.3 \text{ Am}^2$  for various control operations in a similar scenario.

The other consideration is the amount of torque that can be generated by using the torquers and how rapidly we can perform operations on-board the satellite. In a target tracking operational mode we will be using the reaction wheels for pointing and the magnetic torquers to compensate for any residual fields on-board the satellite. However, operating the reaction wheels results in them becoming saturated over time because the need to compensate for various disturbances. Because of this magnetorquers in pointing mode are needed to desaturate the wheels and the speed of desaturation should be minimised because it limits the duty cycle of mission operations.

The magnetorquers are based on the design of ESTCube-1 magnetorquers and a modified coil winder is used. To generate  $0.4 \text{ Am}^2$  on each axis we place two coils on each axis of the satellite. This means that each coil has to generate a magnetic moment of at least  $0.2 \text{ Am}^2$ . As the area for the coils is limited by the structure to  $80 \times 80 \text{ mm}$  or  $60 \times 120 \text{ mm}$  and the thickness to  $2.5 \text{ mm}$ , then two different coil designs are made. The parameters of the designs are given in Table 3.2 below.

|                                 | Short side coil       | Long side coil        |
|---------------------------------|-----------------------|-----------------------|
| Dimensions ( <i>mm</i> )        | 80 x 80 x 2.5         | 60 x 120 x 2.5        |
| Area ( $m^2$ )                  | $5.557 \cdot 10^{-3}$ | $6.254 \cdot 10^{-3}$ |
| Voltage ( <i>V</i> )            | 7.2                   | 7.2                   |
| Resistance ( $\Omega$ )         | 62                    | 71                    |
| Power Consumption ( <i>MW</i> ) | 835                   | 730                   |
| Current ( <i>mA</i> )           | 116                   | 101.3                 |
| Number of turns                 | 400                   | 400                   |
| Magnetic moment ( $Am^2$ )      | 0.258                 | 0.254                 |

Table 3.2: Magnetorquer parameters for short side and long side coils.

### 3.1.3 Cold gas thrusters

The need for cold gas thrusters comes from the mission requirement to operate the satellite outside of Earth's magnetic field influences. Cold gas thrusters operate by storing the fuel in a liquid state and boiling the fuel to a gaseous state which is then

released. An inverse force generated by the mass exhaust from the satellite is given to the satellite. If the force is not directed towards the centre of mass, then operating the thrusters will also generate a change in angular velocity. Thrusters are used to spin up the satellite in order to generate centrifugal force for the tether deployment experiment.

NanoSpace AB provides the ESTCube team with a micropropulsion system for nanosatellites that can be used for both propulsion and actuation. The thrusters are based on MEMS chips, which help to minimise the size of the system as conventional thrusters are too large for CubeSats. The module uses butane as a propellant.

The thruster has four nozzles, each can provide up to  $1\text{ mN}$  of thrust. As the nozzles are placed on the corners of the module and pointing towards the long axis, then we are still able to use the module to control the angular velocity in 2 axes. The configuration of the nozzles and thrusters used for the main experiment is shown on Figure 3.2.

The basic module is able to provide a total of  $40\text{ Ns}$  of impulse. However, because of our high angular momentum requirements, we added a larger tank to the system, which in the current configuration is able to provide around  $80\text{ Ns}$  of impulse that results in  $2\text{ Nms}$  of angular momentum for the satellite in the current configuration. The total angular momentum is enough to reel out 50 metres of tether. The rest of the angular momentum generation needs to be done using magnetic coils and Coulomb drag in the LEO mission.

For the lunar mission an additional thruster module is required that would have the thrust nozzles tilted at 90 degrees. This would enable 3 times higher angular momentum that is almost enough to deploy 100 metres of tether and the rest of the deployment can be done using the E-sail effect. The tether calculations are given in Appendix A

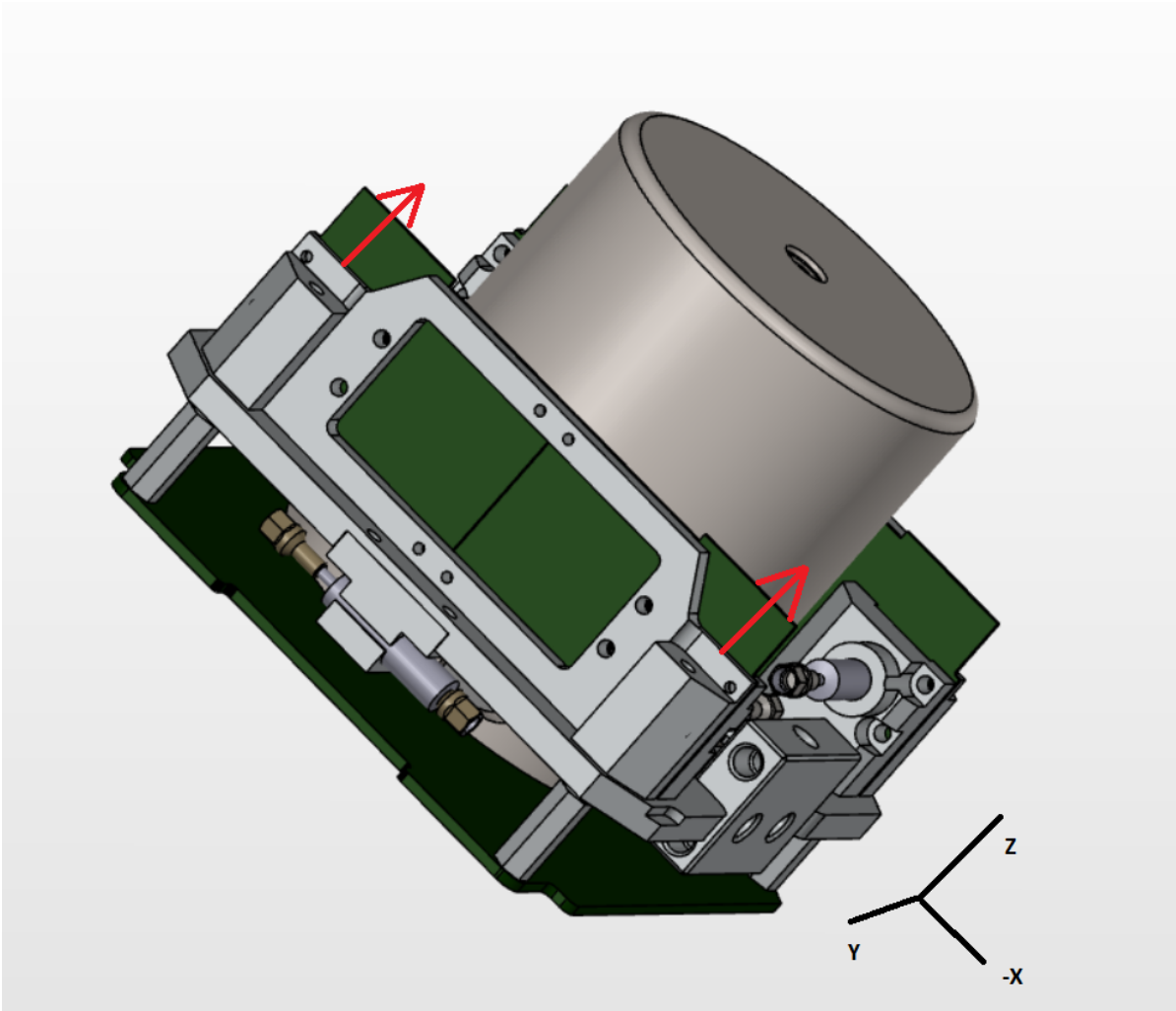


Figure 3.2: Thruster module for ESTCube-2. The thrusters used for spinning up the satellite around x-axis are designated with red arrows. The tank is the large circular structure that holds fuel.

## 3.2 Sensors

### 3.2.1 Sun sensors

Sun sensors are devices that can determine the orientation of a light source. As the brightest light source near Earth is the Sun, then the sensor is designed to measure the direction of Sun. There are two type of Sun sensors – coarse and fine. Coarse sensors are usually used to cover a larger field of view (FOV), however they are more susceptible to

Earth's albedo and have a lower accuracy in general. This is why we are using fine Sun sensors on each side of the satellite, providing full coverage while still achieving higher precision.

The Sun sensors are developed in-house based on the experience obtained during the ESTCube-1 mission (see Section 2.2). The Sun sensor is divided into three parts, the sensor with electronics, body and mask. The sensor is a Hamamatsu S9226-04 linear image sensor [29], the body is an aluminium structure, that is designed to handle the launch vibrations and the space environment and the mask is a  $40\ \mu\text{m}$  wide and  $8\ \text{mm}$  long slit that is placed in front of the sensor.

The image sensor consists of  $1024 \times 1$  pixels, that each are able to detect the amount of light shining on the pixel. The linear image sensor was chosen because it is possible to filter out the albedo from Earth that affects the sensor results. The slit in front of the sensor allows light to illuminate the sensor only from the direction of the light source and using trigonometry it is possible to find out that direction. The results from two sensors on each sidepanel can be combined to create a unit vector that describes the direction of the light.

Different sensor types require different type of mask designs. If the sensor was a PSD, then we would need to make a trade-off between the diffraction from the slit and the beam width. However, as we have a linear image sensor then more alternatives are possible. The easiest way is to make the slit small enough that the light beam width matches one pixel and then use thresholding to find the most illuminated pixel. This would give us up to one pixel accuracy, which for 100 deg FOV sensor would be around 0.1 deg.

An alternative way is to make the slit even smaller, which results in a diffraction pattern created on the sensor. If we are then able to fit the sensor measurements to the diffraction pattern we can get the mean of the diffraction pattern very accurately, which can give us subpixel accuracy when measuring the light source direction. The diffraction pattern created by a  $40\ \mu\text{m}$  slit by sunlight in space is shown on Figure 3.3.

On ESTCube-1, each position sensitive device (PSD) on a Sun sensor was calibrated independently. This was done by rotating the sensor only around one axis, however as described in subsection 2.2.1 this is not sufficient to fully calibrate the sensors. In order

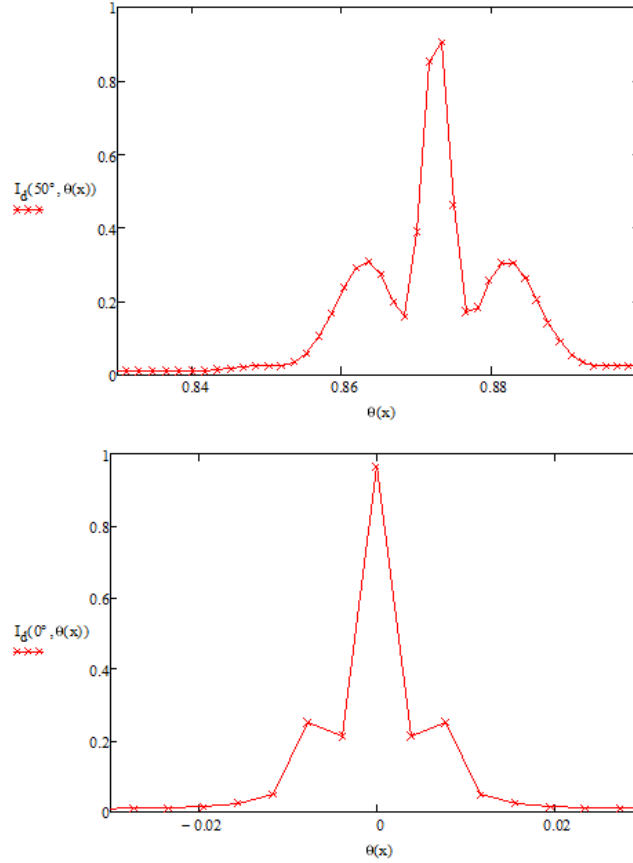


Figure 3.3: Diffraction calculation for Sun sensors. Top plot shows when light illuminates the end of the sensor and the bottom plot when the light illuminates the middle of the sensor. All of the wavelengths from 300 to 1000 nm are integrated together. Currently the sensor optical response is not taken into account. The x-axis represents the sensor length from -1 to 1 with each cross on the image representing one pixel on the sensor and the y-axis represents the intensity for each pixel from 0 to 1

to calibrate the sensors for the sensor misalignment and to create the diffraction pattern fitting function we shall use a solar simulator in Tartu Observatory and turn the Sun sensor in two direction while not changing the distance from the light source in order to not change the intensity that reaches the sensor.

### 3.2.2 Other sensors

In addition to the Sun sensors we use magnetometers, gyroscopes, accelerometers and Star trackers. A short description of those sensors is given below. MEMS based

magnetometers, gyroscopes and accelerometers are commercial off-the-shelf (COTS) components and the star tracker is a in-house built camera that aims to image the stars.

Magnetometers measure the magnetic field strength in 3 axes. This is used to create a magnetic field direction vector, that is used as one source for attitude determination. Magnetometers are susceptible to residual magnetic moments and temperature influences, which need to be compensated for. Magnetometers can not be used in a Lunar orbit.

Gyroscopes measure the angular velocity of the satellite in three axes. Angular velocity is used to propagate the satellite's orientation in time, which is used in the sensor fusion algorithm. They are susceptible to any vibrations on the satellite for example from reaction wheels or the plasma brake unreeling motor. The vibrations create significant noise on the sensor, which is difficult to filter out. In addition the gyroscope offset and gain are both susceptible to temperature that needs to be calibrated out and the MEMS based gyroscopes experience a zero-offset drift.

Accelerometers measure the acceleration of the satellite. They are used for the closed loop control of thrusters for orbit manoeuvring and torque control.

A star tracker is used to take an image of the stars, find the star coordinates from the image and match those coordinates with a database. A star tracker provides very accurate attitude information, but the processing takes time and the algorithms do not work at high spin rates.

At higher spin rates the star tracker could be used as a limb detector. The limb of a planetary body can be used as one attitude measurement for the determination process. In lunar orbit there is not enough information to fully determine our attitude without limb detection or star tracking, because we lack magnetic field information.

# 4 Attitude Determination

This chapter describes the theoretical background for attitude determination and describes how the spacecraft is modelled so that the attitude determination can be further tested. The reasoning for using quaternions is presented, the way how to calculate attitude using vector measurements is given and the various models used for simulating the satellite in the simulation environment, used in attitude determination processes and sensor models used for data generation are presented.

## 4.1 Attitude

Attitude is the representation of the satellite's orientation with respect to an external reference frame. In the satellite's case, the attitude is usually given with a reference to a planetary body such as Earth. This orientation for a satellite in an Earth orbit is represented as the rotation from the satellite reference frame into the Earth-centered inertial (ECI) frame. The ECI frame is defined so that the origin is at the centre of Earth, the x-axis is permanently fixed on a specific location on the celestial sphere and the z-axis is aligned with the Earth's polar axis. The y-axis is fixed so that the frame would follow the right-hand rule [30].

There are different ways to represent the attitude of the satellite, but on ESTCube-2 we are using quaternions. Quaternions have many advantages over other rotation formalisms in our case.

- The quaternions are computationally more efficient than other formalisms, which is important because of the limited hardware of the satellite,

- Quaternions are more easily normalisable, which means they accumulate less errors,
- Quaternions do not have any singularities such as gimbal lock,
- Quaternions are easily interpolated, which can be used to compensate for the sensors phase shift resulting from taking measurements at different times.

## 4.2 Wahba's Problem

Attitude is calculated by comparing the different sensor measurements to their corresponding models. We aim to find the rotation between the satellite inertial reference frame and the ECI frame. The satellite has two type of sensors that are able to measure attitude, the Sun sensors and magnetometers. Both of these sensors do not give us the full information about the rotation of the satellite, as they provide no information of rotating around the vector that they measure.

However, when we have two different measurements we are able to combine these to one attitude solution. This is an error minimisation problem called the Wahba's problem as the two measurements do not exactly align. The cost function that we aim to minimise is described in Equation 4.1, where  $J$  is the cost,  $\mathbf{A}$  is the rotation matrix between the two coordinate systems,  $\mathbf{b}_i$  and  $\mathbf{r}_i$  are the vector measurements in two different coordinate frames (one is the sensor measurement and one is the estimation from an environment model) and  $a_i$  is the weight of the sensor that can be chosen to be the inverse of the measurement noise of the sensor described with the variance [31].

$$J(\mathbf{A}) = \sum_{i=1}^m a_i \|\mathbf{b}_i - \mathbf{A}\mathbf{r}_i\|^2 \quad (4.1)$$

There are various popular ways to solve this equation such as the SVD-method, q-method and the QUEST algorithm. Our current implementation uses the SVD-method, because it is quicker than other methods [32].

In the SVD-method [31] first the Equation 4.1 is transformed into Equation 4.2, where  $\mathbf{B} = \sum_{i=1}^m a_i \mathbf{b}_i \mathbf{r}_i^T$

$$J(\mathbf{A}) = \sum_{i=1}^m a_i - \text{trace}(\mathbf{A}\mathbf{B}^T) \quad (4.2)$$

In order to minimise the cost function, we should maximise the trace. For that one can use singular value decomposition, which is where the name of the method comes from. The singular value decomposition of  $\mathbf{B}$  can be written as

$$\mathbf{B} = \mathbf{U}\mathbf{\Sigma}\mathbf{V}^T = \mathbf{U} \text{diag}[\Sigma_{11}, \Sigma_{22}, \Sigma_{33}] \mathbf{V}^T \quad (4.3)$$

So we can write

$$\text{trace}(\mathbf{A}\mathbf{B}^T) = \text{trace}(\mathbf{U}^T \mathbf{A} \mathbf{V} \text{diag}[\Sigma_{11}, \Sigma_{22}, \Sigma_{33}]) \quad (4.4)$$

As the  $\det(\mathbf{A}) = 1$  because it is a rotation matrix, then we can write the maximisation of trace out as given in the paper [32].

$$\mathbf{U}^T \mathbf{A}_{opt} \mathbf{V} = \text{diag}[1, 1, \det(\mathbf{U})\det(\mathbf{V})] \quad (4.5)$$

We can transform that equation to get the rotation matrix given by

$$\mathbf{A}_{opt} = \mathbf{U} \text{diag}[1, 1, \det(\mathbf{U})\det(\mathbf{V})] \mathbf{V}^T \quad (4.6)$$

Although with this approach it is possible to estimate the attitude of the satellite it faces many issues. These issues will be described in Chapter 5 and the more complex attitude estimation algorithms are described.

### 4.2.1 Models for the satellite

The models in the context of attitude determination can be divided into three main parts: orbit propagation, supporting models for attitude determination and sensor modelling.

Orbit propagation on ESTCube-2 is done using Simplified Perturbations model 4 (SGP4). The SGP4 model calculates the position of the satellite relative to the ECI frame. The error from the SGP4 can be up to 10 km in position which is quite large and already affects the attitude determination accuracy [33]. Currently alternative algorithms are being looked into that have additional error checking like HSGP4, which involves using the position from some ranging capabilities such as our communication system [33].

To obtain attitude information from the magnetometers we need to calculate the Earth's magnetic field vector at the position of the satellite and then compare them to the magnetometer measurements. The Earth's magnetic field is calculated using the IGRF-12 model, which has an average error of 0.22% with a standard deviation of 0.39%. 99.5% of the IGRF predictions are within 2% of the real magnetic field values. As the magnetic field of the Earth has many anomalies, then using the 2% value for uncertainty estimations is useful to estimate the worse case scenario [34].

The Earth's magnetic field model is affected by the Earth rotation model uncertainty in our implementation. The Earth rotation model uncertainty is caused by the Earth nutation of 9.2 arcseconds per 19 years and Earth precession of 50 arcseconds per year [30, p. 27].

To get attitude information out of the Sun sensors we need to calculate the direction of the Sun for the satellite. The Sun direction model implementation has an uncertainty of one arcminute. All of these models uncertainty directly affect the attitude determination accuracy [35].

### 4.3 Sensor Modelling

There are various errors that affect the sensor measurements. In order to accurately test the attitude determination and control, we need to accurately model our sensors. One of the errors that is present in every sensor and that needs to be added is the misalignment of the sensor and the satellite reference frame. This can be caused by different tilts created when soldering the sensor or putting the sensor board in the satellite, as for example Sun sensor boards will not be precisely orthogonal to the sensor board.

This error can be added to the ideal state by creating an error quaternion that describes how the sensor reference frame and the satellite reference frame are misaligned. The sensor measurements are turned using that quaternion. This error is constant for each sensor during one simulation run.

The noise for each sensor can be estimated and added to the sensor readings. The noise is modelled in the current implementation using a Gaussian distribution. There exists a zero-offset that is usually not precisely calibrated for each sensor and needs to be added as an error. Note that for some sensors the zero-offset is caused by factors that we do not have full control and knowledge of such as the residual magnetic moment and the gyroscope drift.

Sensors experience temperature dependent offset and gain changes [22]. The offset change means that there is a temperature dependent function that shifts the output in some direction while the gain results in a function that is dependent on the quantity that we measure. The offset dependency on temperature is described in Equation 4.7, where  $e_1$  is the gain error function and  $e_2$  is the offset error function and the function  $f$  transforms the quantity that the sensor measures into the sensor output.

$$Output = f(x) + f(e_1(t, x)) + f(e_2(t)) \quad (4.7)$$

The sensors needs to be modelled differently to account for sensor specific errors in the measurements. For example, operating the reaction wheels should add noise to the sensor outputs and the residual magnetic moment should be added to the sensors to see how well it is filtered out. The Sun sensors are affected by the Earth's albedo, however modelling albedo is currently not a priority as it will be very difficult to fully simulate the Sun sensor performance. Tests that estimate the performance of the Sun sensors when many light sources are present and a simplified model for that can be considered in the future.

Because the environment models have some uncertainty, then for attitude determination and control algorithm testing purposes we need to add additional noise to these outputs. This is the most likely place where because of the complexity of the models used the normal distribution assumption for the noise might not be accurate, however currently

only normal distribution noises are assumed.

The sensor modelling block is still under development and some of the functions described here are still under development such as the reaction wheel based bias and temperature dependent modelling. These will be implemented in the future to fully test the attitude determination system.

## 4.4 Simulation Environment

The simulation environment involves several different modules that describe the behaviour of the satellite. These modules include the Sun position, satellite position, Earth's magnetic field, disturbance torques, spacecraft dynamics, sensors and actuators.

For ESTCube-2 it was decided to build a new simulation environment, because the old one was not originally written by the ESTCube team and the code was dependent on legacy files that were hard to change. ESTCube is an educational project and learning through implementing the components that describe the attitude determination and control is very helpful for a number of students. The simulation environment is made in MATLAB using the Simulink environment, which is used because it makes the process of changing things and analysing the results using different plots very quick and efficient. The collapsed view of the simulation environment is shown on Figure 4.1.

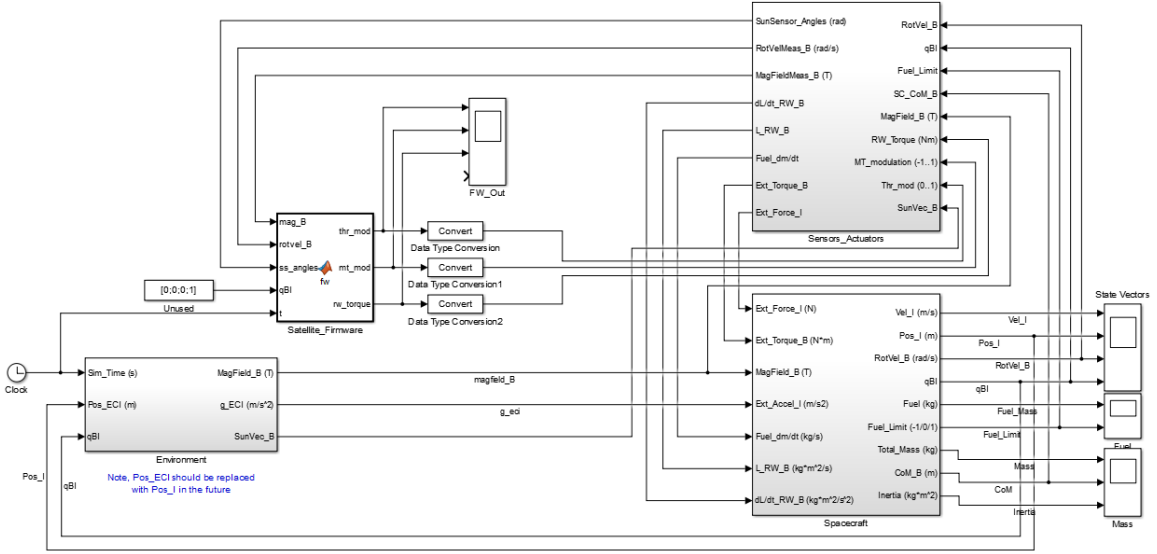


Figure 4.1: The simulation environment collapsed view with various models. The simulation environment given in this Figure is still under development

The spacecraft dynamics is governed by the Euler's equation of rigid body dynamics given in Equation 4.8, where  $\mathbf{I}$  is the inertia tensor,  $\boldsymbol{\omega}$  is the angular velocity,  $\dot{\boldsymbol{\omega}}$  is the change in angular velocity and  $\mathbf{M}$  is the torque affecting the satellite.

$$\mathbf{I} \cdot \dot{\boldsymbol{\omega}} + \boldsymbol{\omega} \times (\mathbf{I} \cdot \boldsymbol{\omega}) = \mathbf{M} \quad (4.8)$$

This equation defines how the satellite is affected by torques and how the angular velocity of the satellite changes when different torques are affecting the satellite. This equation is solved using Simulink built-in solvers

The Equation 4.8 has an important detail, that is easier to see when we write it out into different components in Equations 4.9 to 4.11. The rotation around the Major and Minor inertia axes are stable because when the angular velocity around other axes increases there is a compensating component that aims to minimise that angular velocity. However, when are rotating around the principal axis of inertia that has the intermediate inertia then there is an inverse effect and instead of minimising the angular velocity in other axes, it will start to maximise it.

$$I_1 \cdot \dot{\omega}_1 + (I_3 - I_2)\omega_2\omega_3 = M_1 \quad (4.9)$$

$$I_2 \cdot \dot{\omega}_2 + (I_1 - I_3)\omega_3\omega_1 = M_2 \quad (4.10)$$

$$I_3 \cdot \dot{\omega}_3 + (I_2 - I_1)\omega_1\omega_2 = M_3 \quad (4.11)$$

In the satellite case the principal axes of inertia do not often align with the satellite reference frame as was the case with ESTCube-1. To compensate for that there are two alternatives which both require very accurate determination of the satellite inertia tensor. One of the alternatives is to include the full inertia tensor in all calculations and do the calculations in the satellite reference frame.

The other alternative is to perform the attitude control manouvers and the satellite attitude propagation in the attitude determination algorithm using the principal axes of inertia by converting from and to the satellite reference frame. Currently we have implemented the first case where we are using the full inertia tensor for calculations as it is more intuitive to deal with, however the comparison between the two approaches should be analysed as this has a significant computational impact.

The Simulation environment includes disturbance torques from various effects. These effects include aerodynamic drag, solar pressure, residual magnetic influences and gravity. As a CubeSat is relatively small then the main torque that affects the satellite is the residual magnetic moment. All of these disturbance torque created directly influence the attitude control of the satellite according to the Equation 4.8.

The main issues when generating sensor data using the simulation environment is that the Unscented Kalman Filter is created to filter out noise that has a normal distribution. As normal distribution noises are the easiest to create then the current simulation environment version uses those. However if we are using more advanced algorithms that aim to identify different underlying distributions from the Gaussian distribution, then using the simulated results might give different performance compared to the real world use case.

The simulation environment is used for testing the attitude controller and determination software. In order to make this process more efficient the simulation environment will use a wrapper for the C code that is used on-board the satellite. The reasons for that is

described under Subsection 2.2.2.

The simulation environment can be used for many different starting conditions, which helps us characterise and perform statistical analysis on different algorithms and their performance. Most important parameters to be varied in such an analysis include sensor noises, orbital position (which affects the magnetic field and eclipse), initial attitude and angular velocity.

# 5 Attitude Estimation Algorithms

This chapter describes why to use more complicated attitude estimation algorithms and introduces different algorithms including a novel algorithm based on recursive Bayes estimation for nanosatellite attitude determination. Note that the mathematics given is not meant to be the full description of the filter or a proof of the Kalman filter mathematics, but instead helps to describe the specifics of the filters.

## 5.1 Kalman Filter

There are various issues when using only one set of measurements to calculate the attitude at a specific time position. These include:

- There might not be data available from all of the sensors all the time, this comes from both fundamental reasons for example eclipse of the Sun and from sensor reading errors, which might not give an output. If there is no data from at least two sensors, then it is not possible to estimate attitude by solving the Wahba's problem [32],
- There is noise on the sensor outputs and errors in the sensor models and when taking a single measurement this noise will also be in the attitude output. This means that using only single measurements makes the attitude output less accurate than using other methods described in the following subsections.

Kalman filter is an algorithm that aims to combine measurements taken over time in order to better estimate the state the covariance of the elements at each timestep. This covariance holds the information from the past measurements.

The Kalman filter workflow is given in the Figure 5.1. At each timestep we have an input state called the priori state. In the prediction step we use the information about the physical model to estimate what the state should be according to our current knowledge. Then we use the measurements taken at the same time as the time that was used for the prediction and compare the measurements using some observation model that converts the state to observations.

By comparing and combining the state and the measurements, we are able to estimate a new mean state and a new covariance matrix. The combining is done using Kalman gain, which is an estimation of how accurate is the predicted state compared to the measurements.

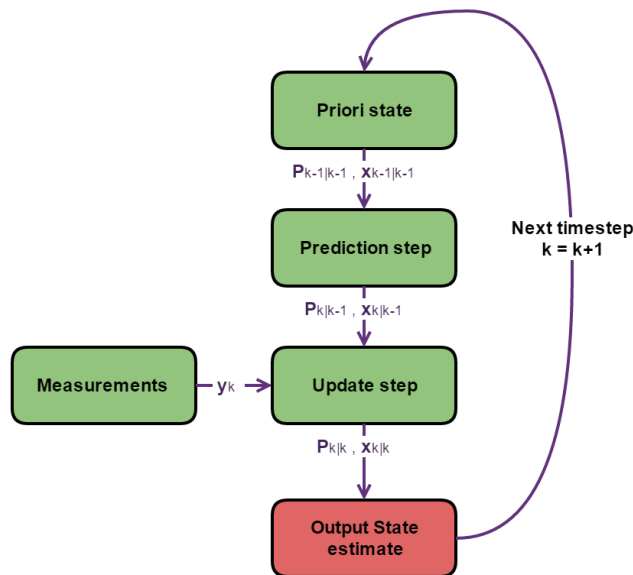


Figure 5.1: The Kalman filter workflow.

A standard Kalman filter has some issues when we want to use it for a satellite. First the most important part is that the standard Kalman Filter only applies for linear systems and the observation and physical models are non-linear. In order to remedy this problem, one can take a look at the Unscented Kalman filter that was also used on ESTCube-1.

## 5.2 Unscented Kalman Filter

The Unscented Kalman filter is an extension of the Kalman filter to solve for problems that include non-linearity [36]. The main idea behind it is to use a set of carefully selected points and propagate those through the true non-linear system. When the points are selected correctly it will capture the true mean and covariance of the system. The points that represent the Gaussian distribution of the state are called sigma points and are described using Equations 5.1 to 5.2, where  $L$  is the number of dimensions (variables) in the state.

$$\chi_{k-1|k-1}^0 = \mathbf{x}_{k-1|k-1}^a \quad (5.1)$$

$$\chi_{k-1|k-1}^i = \mathbf{x}_{k-1|k-1}^a + \left( \sqrt{(L + \lambda) \mathbf{P}_{k-1|k-1}^a} \right) \quad , \quad i = 1, \dots, L \quad (5.2)$$

$$\chi_{k-1|k-1}^i = \mathbf{x}_{k-1|k-1}^a - \left( \sqrt{(L + \lambda) \mathbf{P}_{k-1|k-1}^a} \right) \quad , \quad i = L + 1, \dots, 2L \quad (5.3)$$

$\lambda$  is given using the equation 5.4, where  $\alpha$  and  $\kappa$  describe the spread of the sigma points [31].

$$\lambda = \alpha^2(L + \kappa) - L \quad (5.4)$$

In our implementation we calculate the first priori state using the SVD-method. This makes the initial state closer to the real state and that means the UKF achieves accurate results with less time. The SVD-method is only run when there is data from all of the sensors present, otherwise the filter restarts at the next loop. The UKF workflow is given on Figure 5.2.

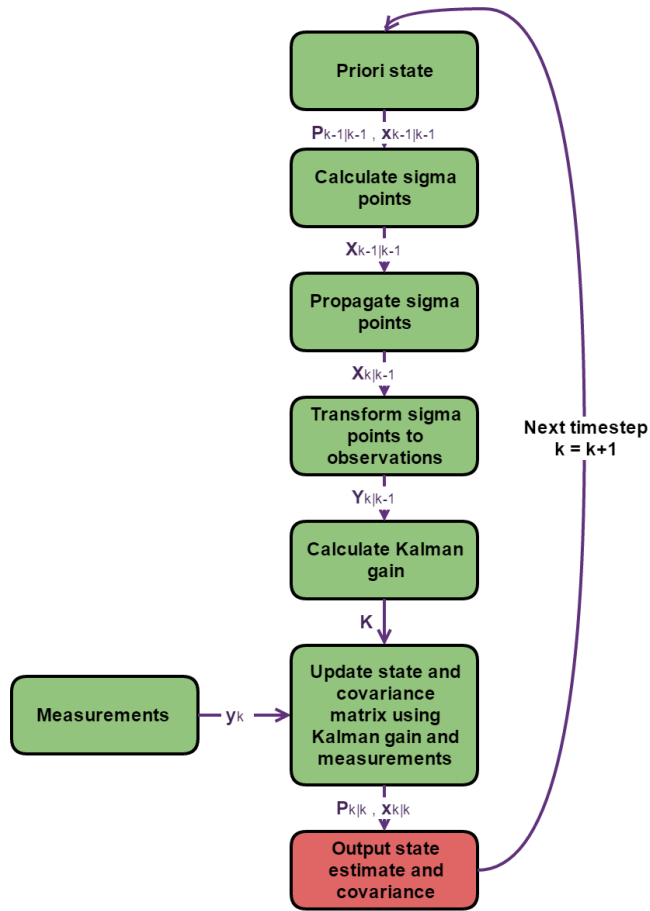


Figure 5.2: The Unscented Kalman filter workflow.

From the priori state a set of sigma points is calculated according to the equations given above. The sigma points are propagated using the Runge-Kutta fourth-order method according to Euler's equation for rigid body dynamics (Equation 4.8), while taking into account any additional torques acting on the satellite, for example, from the residual magnetic moment and from the actuators.

Each Sigma point is propagated to time  $k$  from  $k-1$  and then combined using the weights for each particle using the equations 5.5 and 5.6, where  $\chi$  represents the sigma points, the  $\mathbf{x}$  represents the mean state vector and the  $\mathbf{P}$  represents the covariance matrix.

$$\mathbf{x}_{k|k-1} = \sum_{i=0}^{2L} W_i^m (\chi_{k|k-1})_i \quad (5.5)$$

$$\mathbf{P}_{k|k-1} = \sum_{i=0}^{2L} W_i^c ((\chi_{k|k-1})_i - \mathbf{x}_{k|k-1}) ((\chi_{k|k-1})_i - \mathbf{x}_{k|k-1})^T + \mathbf{Q}_k \quad (5.6)$$

The weights  $\mathbf{W}$  are defined by Equations 5.7 to 5.9 , where  $\beta$  is 2 in the case of a Gaussian distribution [36].

$$\mathbf{W}_s^0 = \frac{\lambda}{L + \lambda} \quad (5.7)$$

$$\mathbf{W}_c^0 = \frac{\lambda}{L + \lambda} + (1 - \alpha^2 + \beta) \quad (5.8)$$

$$\mathbf{W}_s^i = \mathbf{W}_c^i = \frac{1}{2(L + \lambda)} \quad (5.9)$$

After we have found the mean state vector, we can use the observation model to transform it into the observations. The observation models in our case are the Sun position model and Earth's magnetic field model, which require the position of the satellite. This conversion is not precise as the models have errors in them.

Next we need to calculate the Kalman gain, which estimates how accurate the measurements are and how much should they be used when combining them with the prediction. Kalman gain  $\boldsymbol{\kappa}$  is calculated using the predicted measurement covariance  $\mathbf{P}_{y_k y_k}$  and the state-measurement cross-covariance matrix between predicted measurements and predicted state  $\mathbf{P}_{x_k y_k}$  using Equation 5.10. The state vector and covariance matrix are updated according to Equation 5.11 and 5.12.

$$\boldsymbol{\kappa} = \mathbf{P}_{x_k y_k} \mathbf{P}_{y_k y_k}^{-1} \quad (5.10)$$

$$\mathbf{x}_k = \mathbf{x}_k^- + \boldsymbol{\kappa} (\mathbf{y}_k - \mathbf{y}_k^-) \quad (5.11)$$

$$\mathbf{P}_k = \mathbf{P}_k^- - \boldsymbol{\kappa} \mathbf{P}_{y_k y_k} \boldsymbol{\kappa}^T \quad (5.12)$$

The state vector  $\mathbf{x}$  holds 13 components in our implementation. The first four

components are the quaternion elements, the next three are the angular velocity, then three magnetometer bias values and finally three gyroscope bias values. The bias values are linear biases for every axis that are added when converting the state vector in the observation model to sensor values.

In the magnetometer case the bias should estimate the residual magnetic moment of the satellite and other disturbances and in the gyroscope case the bias should estimate the gyroscope drift and any zero offset that might be present in the gyroscope due to various effects such as temperature.

### 5.3 Unscented Particle Filter

The Unscented Particle Filter (UPF) aims to even more accurately estimate the state vector. In the UKF the proposal distribution is always Gaussian and the points are sampled by a rigid method. There are alternative approaches on how to prevent this Gaussian assumption for example using particle filters. However, particle filters are very computationally expensive and can not be used on a nanosatellite with the frequency that we require as each particle needs to be propagated through the physical model and this is computationally very expensive. The UPF aims to combine the propagation from the UKF and the concept of the particle filter in order to get a better estimation of the covariances and the state vector.

The filter workflow is described under Figure 5.3. In the first timestep the SVD-method is used to get a first estimation of the proposal distribution for the state vector. The proposal distribution is assumed to be Gaussian in the first timestep. Then we sample (using for example Monte Carlo sampling, as this distribution might not be Gaussian in the future) a number of points from the distribution that each runs the UKF algorithm.

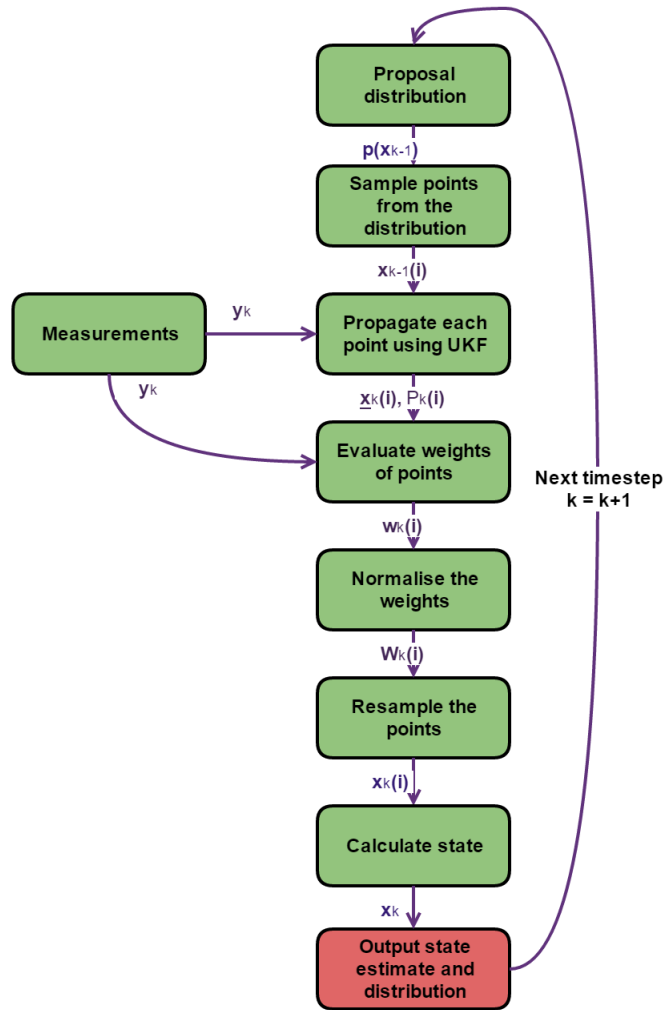


Figure 5.3: The Unscented Particle filter workflow.

After we have propagated each of the particles we combine them by calculating the weights for each particle and then the weights are normalised. The weights are then resampled, which means the particles with high weights are multiplied and particles with low weights are eliminated. In the end the particles will be distributed according to a new distribution that is based on the most recent measurements and the previous distribution.

From this we can calculate a new mean value for the state vector and a new covariance matrix to be used in the next step, also we can use the output distribution as a proposal

distribution for the next timestep. The mean value calculated according to the resampled points is the more accurate orientation estimation that we are after with this filter.

The Unscented particle filter is not yet implemented in the code, but it will be one of the filters that we would like to test out to see how quickly it runs and how big is the difference in the accuracy. As we estimated the UPF to be too computationally expensive, we tried to come up with a way to have the same principles in a less computationally intensive algorithm.

## 5.4 Light Unscented Particle Filter

The Light Unscented Particle Filter (LUPF) is an algorithm in development for ESTCube-2 which aims to reduce the computational complexity of the UPF and increase accuracy of the attitude determination from the UKF. The main idea is similarly with UPF to have non-Gaussian distributions for the state.

The difference is that instead of propagating all of the particles through the UKF, we aim to do the propagation only using one UKF step and then change the output normal distribution. This is done according to sampled points from that normal distribution that are weighed by comparing them to the measurements.

This weighted particle set gives us a more accurate estimation of the mean of the state vector if the underlying distribution is not Gaussian and should therefore give us a more accurate attitude estimation. The workflow of the algorithm is described in Figure 5.4.

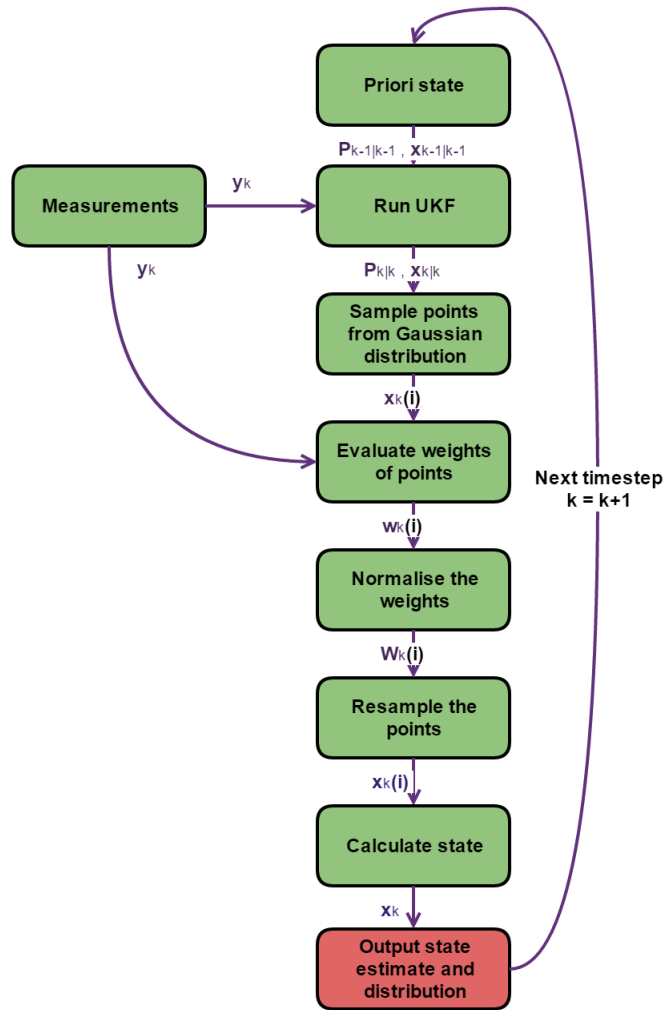


Figure 5.4: The Light Unscented Particle filter workflow.

The main issue is that the output distribution can not be given back to the UKF as it requires a Gaussian proposal distribution as an input and when we do propagation using UKF we always get an output of a normal distribution. The shape of the distribution is important, because when the original distribution that the points are sampled from is closer to the real distribution then less points are needed to estimate the real underlying distribution.

A solution for the fact that the shape of the distribution is not memorised has not been implemented yet. However, the current idea is to use a convolution to the normal

distribution that is predicted by the UKF step. The convolution should transform the normal distribution to the underlying distribution estimated during the particle step and is done before each sampling of particles.

The current state of the algorithm has been implemented in C and is running on a development board of the MCU that is used for the calculations on the satellite. This helps us to optimise the performance when using the algorithm on the satellite. There are still some bugs in the implementation and the algorithm design is being worked on.

Additionally, new sensor measurements could be added to the filter such as the star tracker and temperature sensor information. A filter based on a similar concept was discovered by the author during research for this thesis [37], which gives us extra reason to think that our current approach is correct. The author will continue working on the algorithms in his PhD studies.

## 5.5 Filter Testing

In order to test the attitude filters, we can use two different datasets. Firstly, we can use sensor measurements generated by the simulation environment and secondly, we can use the sensor measurements taken with ESTCube-1. The generated measurements have the advantage that we know the real orientation compared with measurements from space. This means that with ESTCube-1 measurements it is a lot harder to estimate the performance of the filter, however the filter performance is more indicative of the real-world conditions.

The test setup and input to the filtering software is shown in Appendix C for the simulated measurements and in Appendix D for ESTCube-1 measurements.

In order to estimate the performance of the filter R scripts were generated that are able to present the root mean square (RMS) error of all of the state vectors, the difference between the result and the ideal state and various normality tests that we can use to see if the particle filter alters the underlying distribution of the filter. An example of the LUPF results on simulated measurements is shown on Figure 5.5. The figure displays the state vector components that consist of four quaternion components, three angular

velocity components, three magnetometer bias components and three angular velocity bias components.

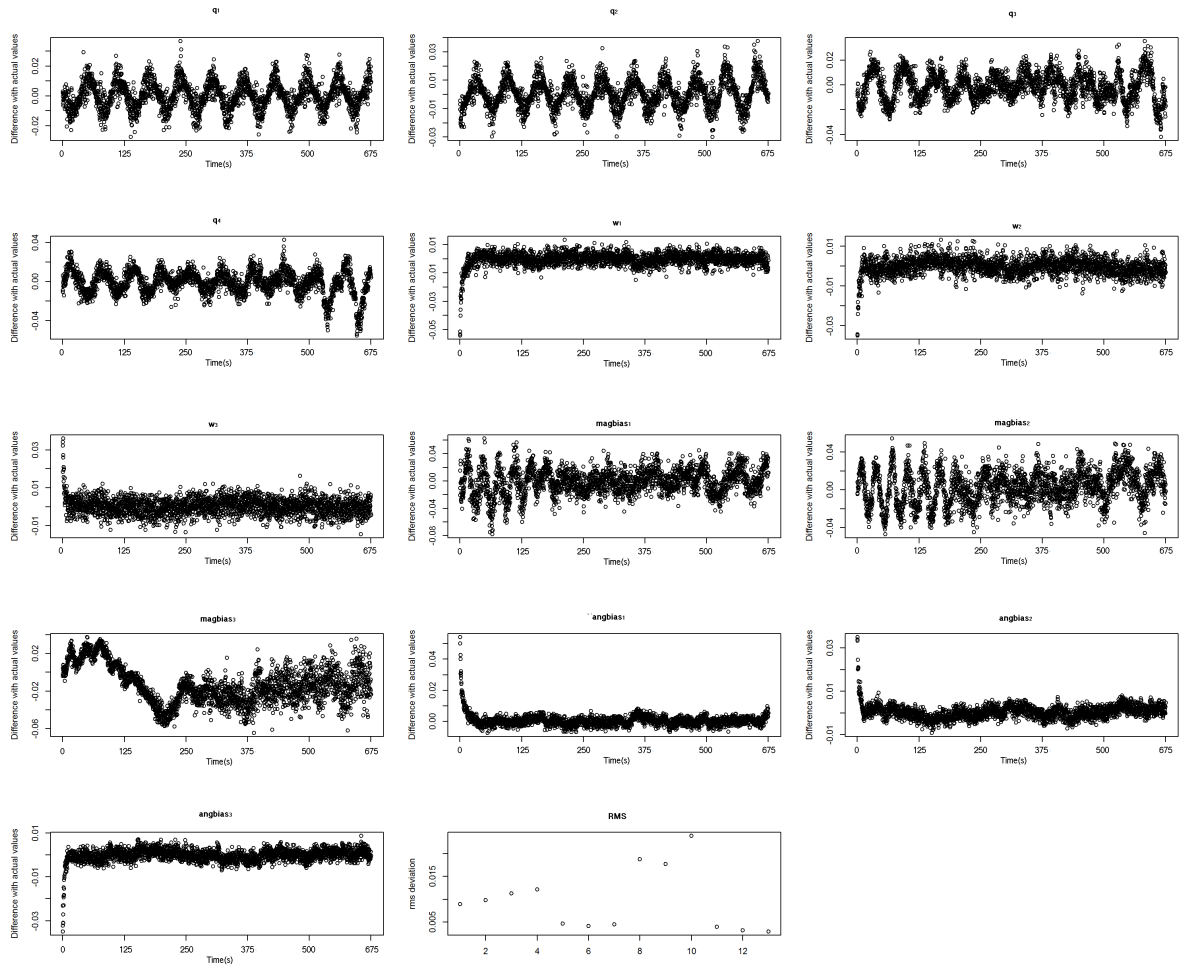


Figure 5.5: The Light Unscented Particle filter results. Each state vector component and the difference with the actual value. The final graph shows the RMS error for all the state vector variables.

In this simulation, the main error source for the measurements was the constant angular velocity bias in all axes and all sensors have measurement noise and errors in them. It is possible to see the angular velocity bias is quickly estimated and the angular velocity

estimation approaches the actual value.

The performance of the UKF for simulated data is almost identical to the performance of the LUPF, which is to be expected because all of the noises modelled in the simulation environment are currently Gaussian.

In order to test the real-world performance of the filter then the measurements from ESTCube-1 were taken and ran on both the UKF and the LUPF. A plot of the quaternion components is shown on Figure 5.6. The spikes are the result of lacking Sun sensor measurements for approximately 30% of the measurements taken as can be seen in Appendix D. The difference between the two filters can be seen on Figure 5.7. The LUPF smooths the jumps in the filter output a small amount, however not significantly.

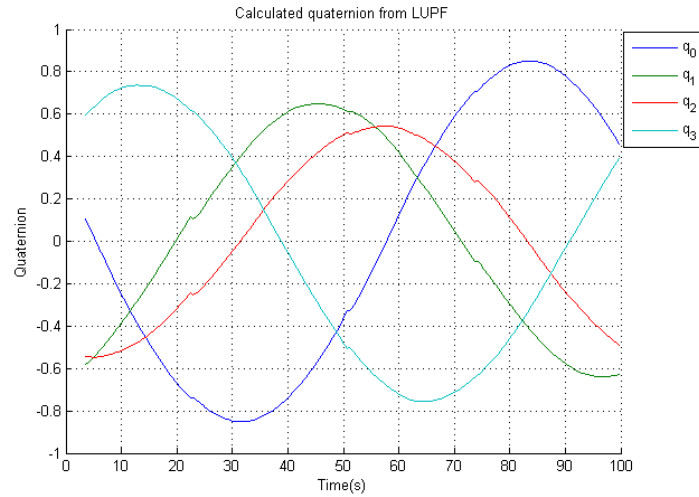


Figure 5.6: The quaternion elements estimated from the ESTCube-1 sensor data by the LUPF algorithm.

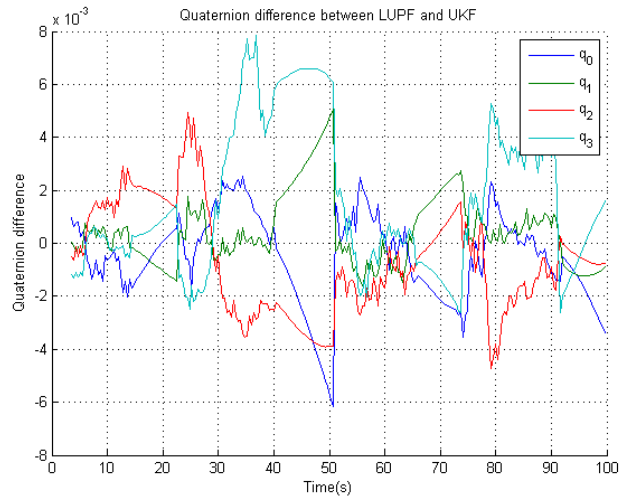


Figure 5.7: The difference between the quaternions from the LUPF and UKF algorithms based on ESTCube-1 sensor data.

The filter requires additional testing and improvements to the LUPF code in order to evaluate if there is a performance advantage for the LUPF over the UKF as the current result is inconclusive.

## 6 Conclusions and future work

This thesis showed the attitude determination and control system design for the ESTCube-2 nanosatellite. The requirements and design drivers were identified and analysis of ESTCube-1 attitude determination and control system results was presented. Additionally, the sensor and actuator designs and choices were described. Finally, the testing and simulation environment for attitude estimation filtering was described and the various filters presented. Some of the initial results for ESTCube-2 attitude determination using the UKF and LUPF were shown.

The AOCS will have functional prototypes for all sensors and actuators described in this thesis during the Summer 2017 so they can be tested and their performance verified.

The simulation environment will be expanded with more detailed sensor simulation, which will be helpful to estimate the differences between the various filters used.

The attitude filtering software requires implementation of various improvements proposed in this thesis such as implementing star tracker and temperature measurements into the filter and other various improvements on the LUPF algorithm. The UPF algorithm will also be implemented for comparison.

# References

- [1] H. Ehrpais, J. Kütt, et al., Nanosatellite spin-up using magnetic actuators: ESTCube-1 flight results, *Acta Astronaut.* (2016) 210–216.
- [2] I. Iakubivskyi, H. Ehrpais, et al., ESTCube-2 mission analysis: plasma brake experiment for deorbiting, in: *International Astronautical Congress*, 2016.
- [3] H. Ehrpais, I. Sünter, et al., ESTCube-2 mission and satellite design, in: *Small Satellites, System and Services Symposium*, 2015.
- [4] N. C. Deschamps, C. C. Grant, et al., The BRITE space telescope: Using a nanosatellite constellation to measure stellar variability in the most luminous stars, *Acta Astronaut.* 65 (2009) 643–650. doi:10.1016/j.actaastro.2009.01.026.
- [5] S. Janson, R. Welle, et al., The NASA optical communications and sensor demonstration program: Initial flight results, in: *Small Satellite Conference*, 2016.
- [6] S. Lätt, A. Slavinskis, et al., ESTCube-1 nanosatellite for electric solar wind sail in-orbit technology demonstration, *Proc. Estonian Acad. Sci.* (2014) 200–209.
- [7] M. Villa, A. Martinez, et al., Cubesat proximity operations demonstration, in: *Small Satellite Conference*, 2015.
- [8] T. Inamori, R. Kawashima, et al., Magnetic plasma deorbit system for nano- and micro-satellites using magnetic torquer interference with space plasma in low earth orbit, *Acta Astronaut.* 112 (2015) 192–199. doi:10.1016/j.actaastro.2015.02.025.
- [9] B. Johnston-Lemke, K. Sarda, et al., BRITE-Constellation: On-orbit attitude performance of a nanosatellite telescope, in: *64th International Astronautical Congress*, 2013.
- [10] P. Janhunen, Electrostatic plasma brake for deorbiting a satellite, *J. Propul. Power* 26 (2010) 370–372. doi:10.2514/1.47537.
- [11] P. Janhunen, A. Sandroos, Simulation study of solar wind push on a charged wire: basis of solar wind electric sail propulsion, *Ann. Geophys.* 25 (2007) 755–767. doi:10.5194/angeo-25-755-2007.
- [12] P. Janhunen, Electric sail for spacecraft propulsion, *J. Propul. Power* 20 (2004) 763–764.

doi:10.2514/1.8580.

- [13] P. Janhunen, P. K. Toivanen, et al., Electric solar wind sail: Toward test missions, *Rev. Sci. Instrum.* 81 (2010) 111301:1–11. doi:10.1063/1.3514548.
- [14] P. Janhunen, Increased electric sail thrust through removal of trapped shielding electrons by orbit chaotisation due to spacecraft body, *Ann. Geophys.* 27 (2009) 3089–3100. doi:10.5194/angeo-27-3089-2009.
- [15] M. Drusch, U. D. Bello, et al., Sentinel-2: ESA’s optical high-resolution mission for GMES operational services, *Remote Sensing of Environment* 120 (2012) 25–36. doi:10.1016/j.rse.2011.11.026.
- [16] F. van der Meer, H. van der Werff, et al., Potential of esa’s sentinel-2 for geological applications, *Remote Sensing of Environment* 148 (2014) 124–133. doi:10.1016/j.rse.2014.03.022.
- [17] P. Janhunen, P. Toivanen, et al., Electric solar wind sail applications overview, *Proc. Estonian Acad. Sci.* 63(2S) (2014) 267–278. doi:10.3176/proc.2014.2S.08.
- [18] A. Slavinskis, M. Pajusalu, et al., Estcube-1 in-orbit experience and lessons learned, in: *Aerospace and Electronic Systems Magazine*, IEEE, 2015, pp. 12–22.
- [19] A. Slavinskis, E. Kulu, et al., Attitude determination and control for centrifugal tether deployment on ESTCube-1 nanosatellite, *Proc. Estonian Acad. Sci.* (2014) 242–249.
- [20] A. Slavinskis, U. Kvell, et al., High spin rate magnetic controller for nanosatellites, *Acta Astronaut.* 95 (2014).
- [21] A. Slavinskis, U. Kvell, et al., Magnetic attitude control algorithms for ESTCube-1, in: *63rd International Astronautical Congress*, 2012. URL: <http://www.iafastro.net/iac/archive/browse/IAC-12/B4/5/14367/>, iSSN: 1995-6258.
- [22] A. Slavinskis, H. Ehrpais, et al., Flight results of ESTCube-1 attitude determination system, *Journal of Aerospace Engineering* (2015) 04015014.
- [23] Gyro mechanical performance: The most important parameter. URL: <http://www.analog.com/media/en/technical-documentation/technical-articles/MS-2158.pdf>.
- [24] T. Ting, K. L. Man, et al., Tuning of kalman filter parameters via genetic algorithm for state-of-charge estimation in battery management system, *The Scientific World Journal* (2014). doi:10.1155/2014/176052.
- [25] Reaction wheel rw1 for pico and nano satellites. URL: [http://www.astrofein.com/2728/dwnld/admin/Datenblatt\\_RW1.pdf](http://www.astrofein.com/2728/dwnld/admin/Datenblatt_RW1.pdf).
- [26] Hyperion technologies 210 series reaction wheel. URL: [http://hyperiontechnologies.nl/wp-content/uploads/2016/08/HT-RW210\\_V1.01\\_Flyer.pdf](http://hyperiontechnologies.nl/wp-content/uploads/2016/08/HT-RW210_V1.01_Flyer.pdf).
- [27] Picosatellite reaction wheels (rw-0.01). URL: <http://www.sinclairinterplanetary.com/reactionwheels/10%20mNm-sec%20wheel%202016a.pdf?attredirects=0>.

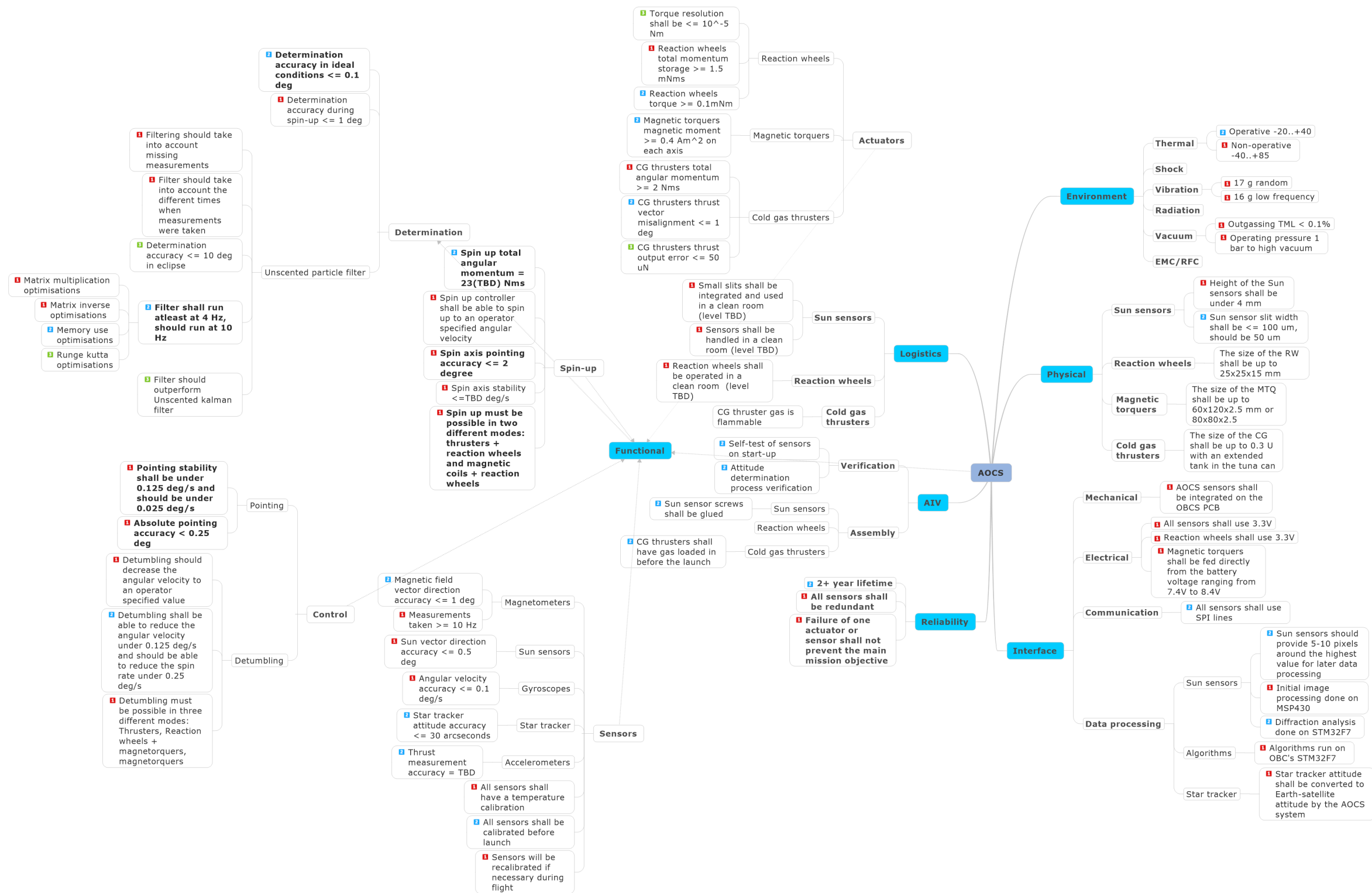
- [28] CubeSat design specification revision 13. URL: [https://static1.squarespace.com/static/5418c831e4b0fa4ecac1bacd/t/56e9b62337013b6c063a655a/1458157095454/cds\\_rev13\\_final2.pdf](https://static1.squarespace.com/static/5418c831e4b0fa4ecac1bacd/t/56e9b62337013b6c063a655a/1458157095454/cds_rev13_final2.pdf).
- [29] Hamamatsu S9226-04 product specification. URL: [http://www.hamamatsu.com/resources/pdf/ssd/s9226\\_series\\_kmpd1121e.pdf](http://www.hamamatsu.com/resources/pdf/ssd/s9226_series_kmpd1121e.pdf).
- [30] J. R. Wertz (Ed.), *Spacecraft Attitude Determination and Control*, Kluwer Academic Publishers, 1978. ISBN: 978-9027712042.
- [31] K. F. Jensen, K. Vinther, *Attitude Determination and Control System for AAUSAT3*, Master's thesis, Aalborg University, 2010.
- [32] F. L. Markley, M. Daniele, Quaternion attitude estimation using vector observations, *Journal of the Astronautical Sciences* 48 (2000) 359–380.
- [33] J. F. San-Juan, I. Perez, et al., Hybrid sgp4 orbit propagator, *Acta Astronaut.* (2017).
- [34] N. Matteo, Y. Morton, Ionosphere geomagnetic field: Comparison of IGRF model prediction and satellite measurements 1991-2010, *Radio Science* 46 (2011).
- [35] O. Montenbruck, T. Pflieger, *Astronomy on the Personal Computer*, 2 ed., Springer-Verlag, 1994. ISBN: 978-3-540-67221-0.
- [36] E. A. Wan, R. V. D. Merwe, The unscented kalman filter for nonlinear estimation, in: *Adaptive Systems for Signal Processing, Communications, and Control Symposium*, IEEE, 2000.
- [37] Y. zheng Zhao, An improved unscented particle filter with global sampling strategy, *Journal of Computational Engineering* (2014) 6. doi:10.1155/2014/175820.

## 7 Appendices

# A Tether Deployment Calculator

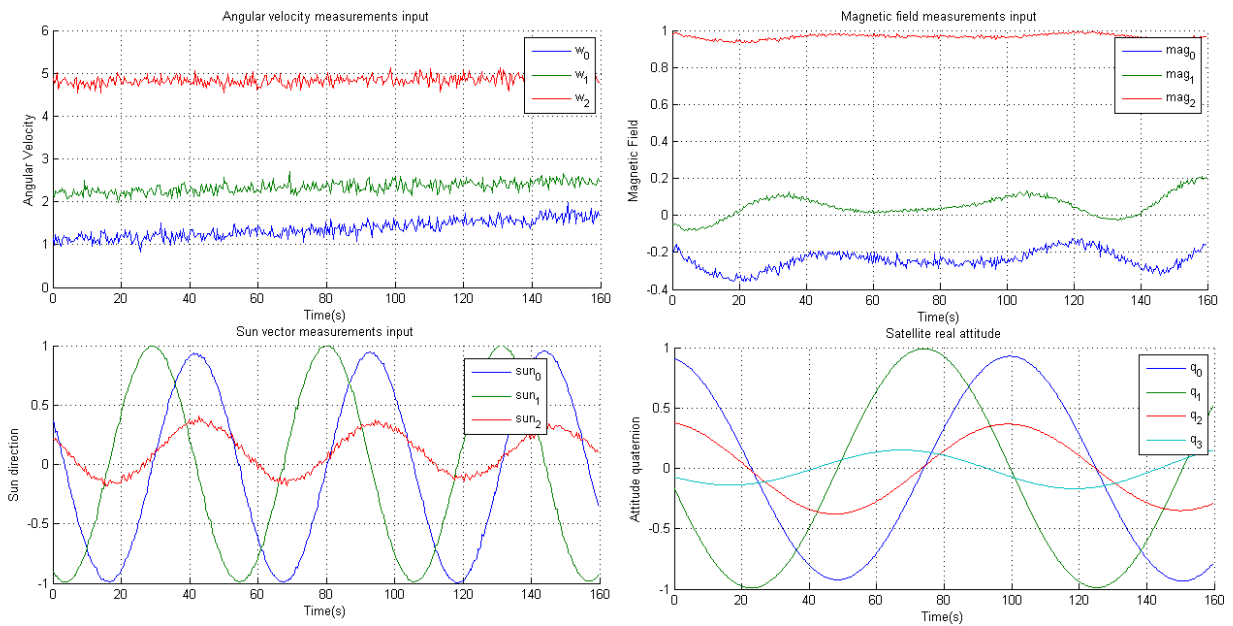
| Satellite           |              |                    |  |  |             |                    |  |  |            |                  |              |
|---------------------|--------------|--------------------|--|--|-------------|--------------------|--|--|------------|------------------|--------------|
| sat mass            | 4.000E+00    | kg                 |  | Green is input, blue is calculated value |             |                    |  |  |            |                  |              |
| sat dim 1           | 340.000E-03  | m                  |  |  |             |                    |  |  |            |                  |              |
| sat dim 2           | 100.000E-03  | m                  |  |  |             |                    |  |  |            |                  |              |
| sat inertia         | 41.867E-03   | kg*m <sup>2</sup>  | $m/12 * (w^2 + h^2)$                                       |  |             |                    |  |  |            |                  |              |
| Target Tether       |              |                    |  | Initial Tether                           |             |                    |  | For target length  |            |                  |              |
| length              | 100.000E+00  | m                  |  | ini length                               | 10          | m                  |  |  |            |                  |              |
| weight / m          | 75.000E-06   | kg / m             |  | weight / m                               | 75.000E-06  | kg / m             |  |  |            |                  |              |
| weight              | 7.500E-03    | kg                 |  | weight                                   | 750.000E-06 | kg                 |  |  |            |                  |              |
| endmass             | 2.500E-03    | kg                 |  | endmass wgt                              | 2.500E-03   | kg                 |  |  |            |                  |              |
| inertia             | 50.000E+00   | m <sup>2</sup> *kg | $(m(\text{tether}) * L^2)/3 + m(\text{endmass}) * r^2 [1]$ | inertia                                  | 275.000E-03 | m <sup>2</sup> *kg |  |  |            |                  |              |
| tether tension [2]  | 1.000E-03    | kgf                |  | tether tension                           | 1.000E-03   | kgf                |  | tether tension   | 1.147E+00  | kgf              |              |
| tether tension      | 9.810E-03    | N                  | kgf * 9.81   | tether tension                           | 9.810E-03   | N                  |  | tether tension   | 11.255E+00 | N                |              |
| radial acceleration | 981.000E-03  | m/s <sup>2</sup>   | tension (force) / mass                                     | radial acceleration                      | 3.018E+00   | m/s <sup>2</sup>   |  | radial acceleration  | 3.463E+03  | m/s <sup>2</sup> |              |
| CoM distance        | 62.500E+00   | m                  |  | CoM distance                             | 8.846E+00   | m                  |  |  |            |                  |              |
| Target Total        |              |                    |  | Initial Total                            |             |                    |  | For target length  |            |                  |              |
| ang vel             | 125.284E-03  | rad/s              | $\text{sqrt}(a / r)$                                       | ang vel                                  | 584.138E-03 | rad/s              |  | ang vel  | 19.786E+00 | rad/s            |              |
| ang vel             | 7.178E+00    | deg/s              |  | ang vel                                  | 33.469E+00  | deg/s              |  | ang vel  | 1.134E+03  | deg/s            |              |
| ang mom             | 6.269E+00    | Nms                | $w * l$  | ang mom                                  | 185.094E-03 | Nms                |  | ang mom  | 6.269E+00  | Nms              |              |
| Confirm ang vel     | 0.1252836781 | rad/s              |  |  |             |                    |  |  |            |                  |              |
| Acceleration        |              |                    |  | Acceleration                             |             |                    |  | Time to spin   |            |                  |              |
| attachment point    | 150.000E-03  | m                  |  | attachment point                         | 150.000E-03 | m                  |  | Time to spin   | 22.258E+03 | s                | at max accel |
| max deflection      | 174.533E-03  | rad                | 10 deg   | max deflection                           | 174.533E-03 | rad                |  | Time to spin   | 6.183E+00  | h                | at max accel |
| max ang accel       | 6.534E-06    | rad/s <sup>2</sup> |  | max ang accel                            | 862.690E-06 | rad/s <sup>2</sup> |  | Not for very small tether lengths and tensions               |            |                  |              |
| max ang accel       | 374.393E-06  | deg/s <sup>2</sup> |  | max ang accel                            | 49.429E-03  | deg/s <sup>2</sup> |  | Spin-up in ONE step. Does not consider tether tension limit. |            |                  |              |

## B Requirements mindmap for the AOCS subsystem



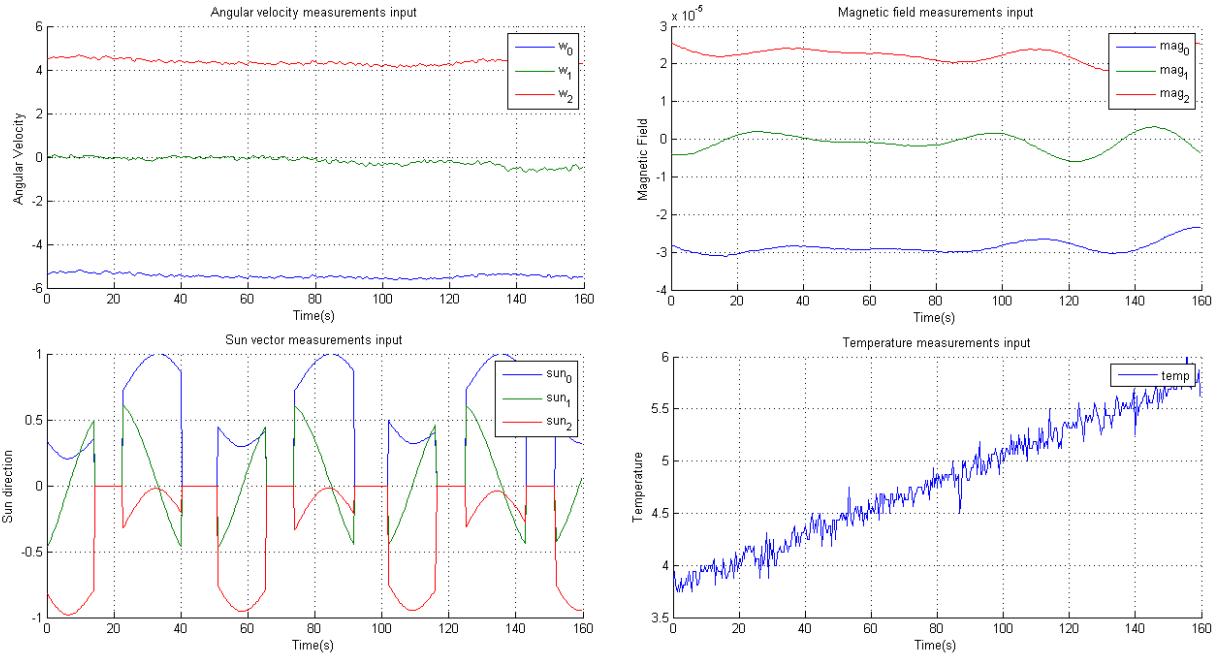
# C Input for UKF vs LUPF filter tests using simulated data

The first 400 datapoints of the input into the UKF and LUPF generated using the simulation environment. The ideal quaternion is also shown.



# D Input for UKF vs LUPF filter tests with EC1 data

The first 400 datapoints taken from the ESTCube-1 measurements that have been averaged and the temperature corrections made. The temperature for the system is also shown



# Lihtlitsents lõputöö reprodutseerimiseks ja lõputöö üldsusele kättesaadavaks tegemiseks

Mina, Hendrik Ehrpais

1. annan Tartu Ülikoolile tasuta loa (lihtlitsentsi) enda loodud teose

## **ESTCube-2 attitude and orbit control system design**

mille juhendaja on Andris Slavinskis

- (a) reprodutseerimiseks säilitamise ja üldsusele kättesaadavaks tegemise eesmärgil, sealhulgas digitaalarhiivi DSpace-is lisamise eesmärgil kuni autoriõiguse kehtivuse tähtaja lõppemiseni;
  - (b) üldsusele kättesaadavaks tegemiseks Tartu Ülikooli veebikeskkonna kaudu, sealhulgas digitaalarhiivi DSpace'i kaudu kuni autoriõiguse kehtivuse tähtaja lõppemiseni.
2. olen teadlik, et punktis 1 nimetatud õigused jäävad alles ka autorile;
  3. kinnitan, et lihtlitsentsi andmisega ei rikuta teiste isikute intellektuaalomandi ega isikuandmete kaitse seadusest tulenevaid õigusi.

Tartu, **17.05.2017**